CHANG-ES. XX. High-resolution Radio Continuum Images of Edge-on Galaxies and Their AGNs: Data Release 3

Judith Irwin, Theresa Wiegert, Alison Merritt, Marek Weżgowiec, Lucas Hunt, Alex Woodfinden, Yelena Stein, Ancor Damas-Segovia, Jiangtao Li, Q. Daniel Wang, et al.

The Astronomical Journal, 158:21 (22pp), 2019 July https://doi.org/10.3847/1538-3881/ab25f6

CHANG-ES. XX. High-resolution Radio Continuum Images of Edge-on Galaxies and Their AGNs: Data Release 3

Judith Irwin[2], Theresa Wiegert[2], Alison Merritt[2], Marek Weżgowiec[3,4], Lucas Hunt[5], Alex Woodfinden[2], Yelena Stein[4,6], Ancor Damas-Segovia[7], Jiangtao Li[8], Q. Daniel Wang[9], Megan Johnson[5], Marita Krause[10], Ralf-Jürgen Dettmar[4], Jisung Im[2], Philip Schmidt[10], Arpad Miskolczi[4], Timothy T. Braun[11], D. J. Saikia[12], Jayanne English[13], and Mark Richardson[13,1]
[1] McDonald Institute, 64 Bader Lane, Queen's University, Kingston, ON K7L 3N6, Canada; Mark.Richardson@queensu.ca
[2] Department of Physics, Engineering Physics & Astronomy, Queen's University, Kingston, ON, K7L 3N6, Canada; irwinja@queensu.ca, theresa.wiegert@gmail.com, merritt.j.alison@gmail.com, 17aw14@queensu.ca, j4im@uwaterloo.ca
[3] Obserwatorium Astronomiczne Uniwersytetu Jagiellońskiego, ul. Orla 171, 30-244 Kraków, Poland; markmet@oa.uj.edu.pl
[4] Faculty of Physics & Astronomy, Astronomical Institute, Ruhr-University Bochum, D-44780 Bochum, Germany; miskolczi@astro.rub.de, dettmar@astro.ruhr-uni-bochum.de
[5] US Naval Observatory, Astrometry Department, 3450 Massachusetts Ave. NW, Washington 20392 D.C., USA; lrhunt87@gmail.com, meg7770@yahoo.com
[6] Centre de Données astronomiques de Strasbourg, Observatoire de Strasbourg 11, rue de l'Université—F-67000 Strasbourg, France; yelena.stein@astro.unistras.fr
[7] Departamento de Astronomía Extragaláctica, Instituto de Astrofísica de Andalucia, Glorieta de la Astronomía sn, E-18008, Granada, Spain; adamas@iaa.es
[8] Department of Astronomy, University of Michigan, 409 West Hall, 1085 S. University, Ann Arbor, MI 48109, USA; jiangtal@umich.edu
[9] Department of Astronomy, University of Massachusetts, 710 North Pleasant St., Amherst, MA 01003, USA; wqd@astro.umass.edu
[10] Max-Planck-Institut für Radioastronomie, Auf dem Hügel 69, D-53121, Bonn, Germany; mkrause@mpifr-bonn.mpg.de, pschmidt@mpifr-bonn.mpg.de
[11] Department of Physics and Astronomy, University of New Mexico, 1919 Lomas Boulevard NE, Albuquerque, NM 87131, USA; ttbraun@unm.edu
[12] Inter-University Centre for Astronomy and Astrophysics, Post Bag 4, Ganeshkhind, Pune, Maharashtra, 411007, India; djsaikia21jan@gmail.com
[13] Department of Physics & Astronomy, University of Manitoba, MB, R3T 2N2, Canada; jayanne_english@umanitoba.ca
Received 2019 March 22; revised 2019 April 24; accepted 2019 May 3; published 2019 June 18

Abstract

The CHANG-ES galaxy sample consists of 35 nearby edge-on galaxies that have been observed using the VLA at 1.6 and 6.0 GHz. Here we present the third data release of our sample, namely, the B configuration 1.6 GHz sample. In addition, we make available the *band-to-band* spectral index maps between 1.6 and 6.0 GHz, the latter taken in the matching resolution C configuration. The images can be downloaded from https://www.queensu.ca/changes. These are our highest-resolution images (≈3″), and we examine the possible presence of low-luminosity active galactic nuclei (AGNs) in the sample, as well as some in-disk structure. New features can be seen in the spectral index maps that are masked in the total intensity emission, including hidden spiral arms in NGC 3448 and two previously unknown radio lobes on either side of the nucleus of NGC 3628. Our AGN detection rate, using only radio criteria, is 55%, which we take as a lower limit because some weaker embedded AGNs are likely present that could be revealed at higher resolution. Archival *XMM-Newton* data were used to search for further fingerprints of the AGNs in the studied sample. In galaxy disks, discrete regions of flat spectral index are seen, likely due to a thermal emission fraction that is higher than the global average.

Key words: radio continuum: galaxies – surveys

Supporting material: figure set

1. Introduction

This paper presents the third data release from the Continuum Halos in Nearby Galaxies—an EVLA Survey (CHANG-ES) program. The Expanded Very Large Array (EVLA) is now known as the Karl G. Jansky Very Large Array (hereafter VLA). CHANG-ES is a large program that has observed 35 nearby edge-on galaxies in B, C, and D configurations of the VLA at two radio frequencies: 6 GHz (hereafter *C* band) and 1.6 GHz (hereafter *L* band). Both frequencies were observed in C and D configurations, and only *L* band was observed in B configuration.

The scientific goals of the project are outlined in Irwin et al. (2012a) and cover a range of topics, including investigating the physical conditions and origin of halos, characterizing cosmic-ray transport and wind speed, measuring Faraday rotation and mapping the magnetic field, probing the in-disk and extraplanar far-infrared/radio continuum relation, and exploring the prevalence of active galactic nuclei (AGNs) in nearby spiral galaxies.

Our first data release (Wiegert et al. 2015) provided D configuration images, including total intensity images at two different *uv*-plane weightings, linear polarization (polarization angle and polarized intensity) images, and *in-band* spectral index maps[14] with their error maps. The data release details are outlined in Wiegert et al. (2015), and images in FITS (Flexible Image Transport System) format can be downloaded from https://www.queensu.ca/changes. The second data release (Vargas et al. 2019) provides FITS files of the Hα images that were used in the thermal/nonthermal separation as described in Vargas et al. (2018). The fourth CHANG-ES data release (Vargas et al. 2019) will include images from our C configuration data at both frequencies (R. Walterbos et al. 2019, in preparation).

This third data release presents the B configuration *L*-band images (hereafter BL). In addition, we include *band-to-band* spectral index maps between matching resolution C configuration *C*-band data (hereafter CC) and the BL data.

Since these data sets represent the highest-resolution observations from the CHANG-ES complement (≈3″), they are ideally suited to investigating compact, well-defined

[14] In-band spectral index maps are formed from the slope of the intensity across a single spectral band.

Table 1
L-band B configuration Observations

Galaxy	R.A. (h m s)	Decl. (° ′)	Distance[a] (Mpc)	Date[b]	SB ID	Prim. Cal.[c]	Zero Pol. Cal.[c]	Sec. Cal.
NGC 660	01 43 02.40	+13 38 42.2	12.3	2012 Jun 24	9833270	3C 48	3C 84	J0204+1514
NGC 891	02 22 33.41	+42 20 56.9	9.1	2012 Jun 24	9833270	3C 48	3C 84	J0230+4032
NGC 2613	08 33 22.84	−22 58 25.2	23.4	2011 Mar 21	3699677	3C 286	OQ 208	J0846−2610
NGC 2683	08 52 41.35	+33 25 18.5	6.27	2012 Jun 16	10459911	3C 286	OQ 208	J0837+2454
NGC 2820	09 21 45.58	+64 15 28.6	26.5	2012 Jun 24	9872780	3C 286	OQ 208	J0921+6215
NGC 2992	09 45 42.00	−14 19 35.0	34	2011 Mar 21	3699677	3C 286	OQ 208	J0943−0819
NGC 3003	09 48 36.05	+33 25 17.4	25.4	2012 Jun 16	10459911	3C 286	OQ 208	J0956+2515
NGC 3044	09 53 40.88	+01 34 46.7	20.3	2011 Mar 21	3699677	3C 286	OQ 208	J1007−0207
NGC 3079	10 01 57.80	+55 40 47.3	20.6	2012 Jun 24	9878453	3C 286	OQ 208	J1035+5628
NGC 3432	10 52 31.13	+36 37 07.6	9.42	2012 Jun 24	9872780	3C 286	OQ 208	J1130+3815
NGC 3448	10 54 39.24	+54 18 18.8	24.5	2012 Jun 23	9878453	3C 286	OQ 208	J1035+5628
NGC 3556	11 11 30.97	+55 40 26.8	14.09	2012 Jun 23	9878453	3C 286	OQ 208	J1035+5628
NGC 3628	11 20 17.01	+13 35 22.9	8.5	2012 Jun 30	3746030	3C 286	OQ 208	J1120+1420
NGC 3735	11 35 57.30	+70 32 08.1	42	2012 Jun 9	9872780	3C 286	OQ 208	J1313+6735
NGC 3877	11 46 07.80	+47 29 41.2	17.7	2012 Jun 17 2012 Jul 4	3752357	3C 286	OQ 208	J1219+4829
NGC 4013	11 58 31.38	+43 56 47.7	16	2012 Aug 11	9888001	3C 286	OQ 208	J1146+3958
NGC 4096	12 06 01.13	+47 28 42.4	10.32	2012 Aug 11	9888001	3C 286	OQ 208	J1331+3030
NGC 4157	12 11 04.37	+50 29 04.8	15.6	2012 Jun 17 2012 Jul 4	3752357	3C 286	OQ 208	J1219+4829
NGC 4192	12 13 48.29	+14 54 01.2	13.55V	2012 Jun 24	3746030	3C 286	OQ 208	J1254+1141
NGC 4217	12 15 50.90	+47 05 30.4	20.6	2012 Aug 11	9888001	3C 286	OQ 208	J1331+3030
NGC 4244	12 17 29.66	+37 48 25.6	4.4	2012 Jun 9	9889954	3C 286	OQ 208	J1227+3635
NGC 4302	12 21 42.48	+14 35 53.9	19.41V	2012 Jul 29	9892023	3C 286	OQ 208	J1254+1141
NGC 4388	12 25 46.75	+12 39 43.5	16.6V	2012 Jul 29	9892023	3C 286	OQ 208	J1254+1141
NGC 4438	12 27 45.59	+13 00 31.8	10.39V	2012 Jul 29	9892023	3C 286	OQ 208	J1254+1141
NGC 4565	12 36 20.78	+25 59 15.6	11.9	2012 Jun 2	9893234	3C 286	OQ 208	J1221+2813
NGC 4594	12 39 59.43	−11 37 23.0	12.7	2011 Mar 17	3693390	3C 286	OQ 208	J1248−1959
NGC 4631	12 42 08.01	+32 32 29.4	7.4	2012 Jun 3	9893234	3C 286	OQ 208	J1221+2813
NGC 4666	12 45 08.59	−00 27 42.8	27.5	2012 Jun 10	9893236	3C 286	OQ 208	J1246−0730
NGC 4845	12 58 01.19	+01 34 33.0	16.98V	2012 Jun 10	9893236	3C 286	OQ 208	J1246−0730
NGC 5084	13 20 16.92	−21 49 39.3	23.4	2011 Mar 17	3693390	3C 286	OQ 208	J1248−1959
NGC 5297	13 46 23.68	+43 52 20.5	40.4	2012 Jun 9	9889954	3C 286	OQ 208	J1327+4326
NGC 5775	14 53 57.60	+03 32 40.0	28.9	2011 Apr 5	3681627	3C 286	OQ 208	J1445+0958
NGC 5792	14 58 22.71	−01 05 27.9	31.7	2011 Apr 5	3681627	3C 286	OQ 208	J1505+0326
NGC 5907	15 15 53.77	+56 19 43.6	16.8	2011 Mar 8	3070258	3C 286	OQ 208	J1438+6211
UGC 10288	16 14 24.80	−00 12 27.1	34.1	2011 Apr 5	3681627	3C 286	OQ 208	J1557−0001

Notes. Observations of the galaxies indicating the pointing center, distance, date, scheduling block (SB), identification number (ID), and primary, zero-polarization leakage, and secondary calibrators. Blanks mean that the value is the same as the previous row.
[a] Distances are from Wiegert et al. (2015). "V" designates a Virgo Cluster galaxy.
[b] "Date" refers to the UT start date.
[c] Alternate names for primary and zero-polarization calibrators: 3C 286 = J1331+3030; 3C 84 = J0319+4130; OQ 208 = QSO B1404+2841 or J1407+2827.

regions in the disk such as star-forming (SF) regions, or AGNs. In this paper, we focus mainly on AGNs, providing an estimate of the AGN frequency in our sample; we also discuss an example of radio emission from a compact region in a galaxy disk.

The galaxies and their positions with adopted distances are given in Table 1.

In Section 2.1, we describe the data acquisition and reductions for the radio and some supplementary X-ray data. Section 3 outlines the images and data products. Section 4 presents some general results from the images. Section 5 lists our criteria for determining the presence of AGNs and compares these results to what has been previously known. Section 6 discusses the galaxy disks and possible contamination from background sources, and Section 7 presents a summary and conclusions.

2. Observations and Data Reductions

2.1. CHANG-ES VLA Data

Table 1 provides observational details for our sample. The observational setup has previously been described in Wiegert et al. (2015) and earlier CHANG-ES papers. The B configuration *L*-band setup was consistent with *L*-band observations in the other VLA configurations. The frequency was centered at 1.575 GHz, with a bandwidth of 512 MHz. The band was split into two sections, the first from 1.247 to 1.503 GHz and the second from 1.647 to 1.903 GHz, with the central gap set to avoid known interference. For all galaxies except NGC 4438, the central frequency was therefore ∼1.58 GHz.[15] For

[15] Very small variations in the central frequency of the resulting images may occur because of the flagging of radio frequency interference (RFI); the FITS header reveals the exact value.

NGC 4438, only the upper half of the frequency band was usable; hence, its central frequency was 1.77 GHz.

The total 512 MHz bandwidth was divided into 32 spectral windows (spws), each with 64 channels, for a total of 2048 spectral channels. The high spectral resolution allowed us to identify and flag interference and was also adopted so that rotation measure (RM) analysis could be carried out at a later date, should the data warrant such an analysis. The spectral resolution also facilitated multifrequency synthesis (e.g., Sault & Conway 1999) and permitted the fitting of an in-band spectral index.

Approximately 2 hr of observing time were allocated for each galaxy. Every galaxy was observed in a "scheduling block" (SB) that included other galaxies so that the total time on each galaxy could be spread out over a wide *uv*-plane range, typically before and after transit. The primary phase and amplitude calibrators (hereafter the primary calibrators) are sources of known flux density for each baseline and frequency, and the secondary phase and amplitude calibrators (hereafter the secondary calibrators) are sources that are closer than 10° from the galaxy in the sky. The secondary calibrator was observed before and after each scan on the target galaxy, and the primary calibrator was observed once per SB. A zero-polarization calibrator was also observed once during an SB for the linear polarization calibration (see below). A list of calibrators is given in Table 1.

The VLA uses right-handed (R) and left-handed (L) circular feeds. Total intensity images (Stokes *I*) are formed from correlation of the parallel hands (RR and LL), and linear polarization images are formed from the correlation of the cross-hands (RL and LR). A summary of the relation between the observed correlations and Stokes parameters is given in Irwin et al. (2018). Each correlation was calibrated separately.

Data reductions were carried out using the *Common Astronomy Software Applications* package, CASA.[16] Irwin et al. (2012b) and Irwin et al. (2013) describe the CHANG-ES data reduction process in detail. Briefly, calibration involved first Hanning-smoothing the data in frequency and correcting for antenna-based delays. The flux density scale was then set using the primary calibrator, and the bandpass response was also corrected using the primary calibrator. Complex gains (amplitudes and phases) were then determined as a function of time using the secondary calibrator. At each step, the data were flagged for interference, as needed, and the process was iterative such that the calibration was redone after each flagging episode. In forming each new correction table, previously determined tables were applied on the fly.

The polarization calibration required, in addition, determining the absolute position angle of the linearly polarized flux based on the known angle of the primary calibrator, determining any residual antenna-based delays for the cross-hands, as well as solving for polarization leakage terms using the zero-polarization calibrator, according to standard practice.[17]

Imaging parameters are provided in Table 2.

Maps of Stokes *I*, *Q*, and *U* were made as follows (for information on Stokes *V*, see Irwin et al. 2018).

The multiscale/multifrequency synthesis (ms-mfs) algorithm (Rau & Cornwell 2011) was applied, including w-projection (Cornwell et al. 2008) and the Cotton-Schwab clean (Schwab 1984). A very wide field image was initially made to identify background sources whose sidelobes could cause cleaning problems. In most cases, depending on the field, at least one full primary beam was finally imaged, and sometimes much more. Two maps were made: one using Briggs robust 0 *uv* weighting as implemented in CASA (Briggs 1995; hereafter referred to as "rob 0" maps), and one using robust 0 weighting with an additional outer Gaussian *uv* taper (hereafter "uvtap" maps or "uvtap" followed by the taper size). The *uv* taper size was adopted so that the uvtap synthesized beam was roughly twice the diameter of the nontapered map. Almost all images used a cell size of 0.″5; hence, the synthesized beam was well sampled. In a few cases, image results and/or efficiency were improved by using 0.75 or 1″ cells.

We attempted self-calibration for most of the galaxies according to the prescription given in Wiegert et al. (2015). For many galaxies, however, the emission was too weak for effective self-calibration. In the end, 15 galaxies were effectively self-calibrated, either phase-only or amplitude and phase together.

During imaging/cleaning, a spectral index is fit across the band, producing maps of the *in-band* spectral index and associated error maps. A fit of the form $I_\nu \propto \nu^\alpha$ is performed; hence, a straight line in log space is fit across the 512 MHz *L*-band bandwidth. A 5σ cutoff was applied when making the in-band spectral index maps, where σ is the rms noise of the total intensity image. Since B configuration emission is generally weak, however, we are not releasing the in-band spectral index maps and instead are releasing *band-to-band*, BL to CC spectral index maps (Section 3.4). Users who wish to obtain the in-band spectral index maps for brighter sources should email the first author of this paper. See also Section 3.4.3 of Wiegert et al. (2015) for more detailed discussion of in-band spectral index errors.

For polarization imaging, we form the linearly polarized intensity, $P_{\rm lin}$, and polarization angle, χ, images from the Stokes Q and U maps according to

$$P_{\rm lin} = \sqrt{Q^2 + U^2 - \sigma_{Q,U}^2} \quad (1)$$

$$\chi = (1/2)\arctan(U/Q), \quad (2)$$

where $\sigma_{Q,U}$ is the rms noise of maps Q and U; no significant difference was found between the Q and U noise. The latter term in Equation (1) makes a zeroth-order correction for the fact that P images are positively biased (e.g., Simmons & Stewart 1985; Everett & Weisberg 2001; Vaillancourt 2006) and is the only correction that is currently implemented in CASA. For maps of χ, we formed two different maps, one using a $3\sigma_{Q,U}$ cutoff and one with a $5\sigma_{Q,U}$ cutoff, for each *uv* weighting.

Finally, we corrected all maps, including in-band spectral index maps, for the new primary beam (PB) following Perley (2016), whose FWHM at our central frequency is 25.′8.

In this paper, we show total intensity images that are uncorrected for the PB (uniform noise) but make measurements from the images that have been corrected for the PB (corrected flux). Both are downloadable from our website.

2.2. XMM-Newton *Data*

To supplement our data and provide additional information about possible AGNs in the sample, we used *XMM-Newton*

[16] See `casa.nrao.edu`.

[17] See https://evlaguides.nrao.edu/index.php?title=Category:Polarimetry.

Table 2
L-band Imaging Parameters

Galaxy	Weighting[a]	Beam Size[b] (arcsec, arcsec, deg)	rms_I[c] (μJy beam^{-1})	$I_{\max}$[d] (mJy beam^{-1})	$\mathrm{rms}_{Q,U}$[e] (μJy beam^{-1})	$P_{\max}$[f] (μJy beam^{-1})	P comments[g] (%)
NGC 660	rob 0	3.39, 3.27, 44.4	24 (1.5×)	245	18.2	134	$P_{\max}/I < 0.5\%$
	uvtap 16	6.14, 5.79, 76.1	28 (1.5×)	299	21.0	132	$P_{\max}/I < 0.5\%$
NGC 891	rob 0	3.15, 2.90, 54.2	16.0	4.91	18.0	89.3	
	uvtap 17	5.69, 5.33, 53.2	17.0	9.91	18.0	87.1	
NGC 2613	rob 0	5.18, 3.02, −179.7	19.6	0.39	18.5	85.3	
	uvtap 16	7.03, 6.05, −3.2	19.4	0.58	16.7	67.8	
NGC 2683	rob 0	3.06, 2.98, 57.8	14.5	1.06	14.6	65.7	
	uvtap 16	5.86, 5.77, 52.5	15.8	1.43	15.4	66.4	
NGC 2820	rob 0	3.23, 3.17, 52.8	16.3	0.87	16.8	73.4	
	uvtap 16	5.95, 5.92, 27.4	18.5	2.16	16.9	60.8	
NGC 2992	rob 0	4.87, 3.57, 16.4	16.5 (1.2×)	84.3	16.7	78.8	
	uvtap 16	6.53, 6.33, −70.3	16.5 (1.3×)	118	15.9	61.9	
NGC 3003	rob 0	3.11, 3.00, 70.1	14.0	0.77	15.1	67.2	
	uvtap 16	5.89, 5.76, 59.2	15.0	1.48	15.5	52.2	
NGC 3044	rob 0	3.67, 3.39, 68.8	15.0	3.36	14.7	71.8	
	uvtap 16	6.54, 5.54, 86.9	16.0	6.26	14.7	67.1	
NGC 3079	rob 0	3.14, 3.00, 58.4	18.0 (3×)	123	16.4 (2×)	436	$P_{\max}/I = 3.8\%$
	uvtap 16	6.01, 5.80, 47.5	25.0 (5×)	172	17.3 (3×)	607	$P_{\max}/I = 1.8\%$
NGC 3432	rob 0	3.20, 3.12, 82.8	21.0	0.46	21.9	96.8	
	uvtap 16	5.95, 5.75, −23.8	24.0	0.84	22.5	97.8	
NGC 3448	rob 0	3.16, 2.98, 63.9	17.0	2.92	16.3	67.1	
	uvtap 17.5	5.59, 5.32, 52.9	18.0	5.94	17.0	60.8	
NGC 3556	rob 0	3.12, 2.98, 58.2	16.0	2.05	16.0	73.9	
	uvtap 17.5	5.56, 5.36, 49.5	16.5	3.47	16.5	75.8	
NGC 3628	rob 0	3.21, 3.13, 3.7	14.5 (1.6×)	79.9	12.5	59.1	
	uvtap 16	6.01, 5.70, 86.2	20.0 (2×)	134	13.9	68.2	
NGC 3735	rob 0	3.24, 3.11, 33.8	16.0	2.08	16.3	77.1	$P_{\max} < 5\sigma_{Q,U}$
	uvtap 16	6.01, 5.92, 27.5	16.5	4.08	15.7	88.3	$P_{\max} > 5\sigma_{Q,U}$
NGC 3877	rob 0	3.01, 2.87, 22.4	11.5	1.26	11.4	50.2	
	uvtap 16	5.99, 5.86, 36.0	11.5	2.10	11.3	44.3	
NGC 4013	rob 0	3.01, 2.90, −84.2	14.0	4.14	13.7	64.4	
	uvtap 16	5.83, 5.79, 81.9	16.0	6.93	14.5	58.0	
NGC 4096	rob 0	3.06, 2.94, −84.9	14.5	0.24	14.8	70.6	
	uvtap 16	5.86 x 5.79, 70.6	14.5	0.55	15.8	76.7	
NGC 4157	rob 0	3.02, 2.84, 29.5	11.7 (2×)	0.57	12.0	52.6	
	uvtap 16	5.98, 5.86, 37.3	12.0 (3×)	1.75	11.5	52.2	
NGC 4192	rob 0	3.21, 3.07, −7.5	14.5 (1.2×)	3.52	14.1	59.5	
	uvtap 16	6.00, 5.68, 83.6	22.0 (1.2×)	6.25	14.2	65.5	
NGC 4217	rob 0	3.07, 2.94, −85.5	14.5	2.21	14.0	58.1	
	uvtap 16	5.86, 5.80, 76.7	15.1	3.94	15.0	57.0	
NGC 4244	rob 0	3.09, 3.00, 45.0	14.4	0.79	22.5	121.4	noise peak
	uvtap 16	5.86, 5.82, 40.0	15.2	1.27	22.5	120.3	noise peak
NGC 4302[h]	rob 0	3.50, 3.13, −8.4	13.5	1.13	12.6	52.7	
NGC 4388[h]	rob 0	3.57, 3.22, −2.1	16.0 (4×)	25.2	12.3	59.0	
NGC 4438[h,i]	rob 0	3.32, 2.91, −6.3	25.0 (1.6×)	35.7	26.0 (1.6×)	306	$P_{\max}/I = 1.1\%$
NGC 4565	rob 0	3.31, 3.01, 45.5	15.0	1.61	14.0	68.0	
	uvtap 17	5.87, 5.36, 50.9	15.0	1.81	14.0	59.1	
NGC 4594	rob 0	4.36, 3.25, −14.0	17.5	70.2	15.6	60.3	
	uvtap 16	6.09, 5.85, 87.7	17.5	71.0	14.4	52.7	
NGC 4631	rob 0	3.40, 3.05, 63.4	16.0	7.56	16.3	81.5	
	uvtap 16	6.08, 5.85, 57.1	20.0	11.2	15.6	68.9	
NGC 4666[h]	rob 0	3.80, 3.48, 39.6	15.0 (1.5×)	4.97	14.0	66.1	
NGC 4845	rob 0	3.51, 3.33, 22.7	18.0 (1.4×)	209	15.0	382	$P_{\max}/I < 0.5\%$
NGC 5084	rob 0	5.63, 2.95, −11.8	17.0 (1.15×)	28.2	17.1	68.9	
	uvtap 16	6.87, 5.86, −8.9	16.0(1.25×)	30.4	14.8	67.8	
NGC 5297	rob 0	3.13, 2.99, 52.8	13.6	0.15	22.5	87.5	
	uvtap 16	5.92, 5.82, 54.0	15.8	0.29	22.9	75.6	
NGC 5775	rob 0	3.65, 3.44, 64.3	14.0	2.14	13.9	62.6	
	uvtap 16	6.47, 5.70, 84.7	18.0	4.94	14.2	67.9	
NGC 5792	rob 0	3.89, 3.42, 48.6	15.0 (1.25×)	4.89	14.3	48.9	
	uvtap 16	6.55, 5.74, 78.6	15.0 (1.25×)	8.95	14.5	47.0	
NGC 5907	rob 0	3.35, 2.79, −4.6	13.5	20.8[j]	12.5	53.8[j]	
	uvtap 16	5.94, 5.72, 2.1	15.7	24.6[j]	10.8	48.6[j]	

Table 2
(Continued)

Galaxy	Weighting[a]	Beam Size[b] (arcsec, arcsec, deg)	rms_I[c] (μJy beam^{-1})	I_{max}[d] (mJy beam^{-1})	$rms_{Q,U}$[e] (μJy beam^{-1})	P_{max}[f] (μJy beam^{-1})	P comments[g] (%)
UGC 10288	rob 0	3.80, 3.58, 66.2	14.0 (1.2×)	0.55[k]	12.7	52.0[k]	

Notes.
[a] Weighting applied in the *uv*-plane: rob 0 = Robust zero; uvtap = Robust zero plus an outer Gaussian *uv* taper, where the number specifies the size in klambda units (see Section 2.1).
[b] Synthesized beam parameters of the total intensity images: major axis, minor axis, position Angle. Values for Stokes Q and U are the same or negligibly different.
[c] rms map noise of the total intensity images prior to primary beam correction. Values in parentheses indicate the factor by which the rms should be multiplied when considering values close to the source (Section 3.1).
[d] Peak specific intensity of the total intensity images, as measured on the galaxy itself, after primary beam correction (Section 3.2).
[e] rms map noise of Stokes Q and U images prior to primary beam correction. Values in parentheses indicate the factor by which the rms should be multiplied when considering values to the source.
[f] Peak linearly polarized specific intensity on the galaxy itself after primary beam correction (Section 3.3).
[g] Comments on polarization for cases in which P_{max} is $>5\,\sigma_{Q,U}$ (Section 3.3).
[h] The *uv*-tapered map was not included since it was of poor quality.
[i] NGC 4438 was made using only half the total bandwidth (spw 16–31 only) for a central frequency of 1.77 GHz.
[j] The peak is at the location of the double-lobed radio source that is superimposed at the far SE of the disk. The peak polarization measurement excluded this region.
[k] The peak value belongs to the southern radio lobe of the background quasar that shines through the galaxy; see Irwin et al. (2013).

archive data and obtained spectra for 19 of our galaxies.[18] All data were processed with the SAS 15.0.0 package (Gabriel et al. 2004). For each observation the event lists for two EPIC-MOS cameras (Turner et al. 2001) and the EPIC-pn camera (Strüder et al. 2001) were filtered for periods of intense background radiation and therefore prepared for the spectral analysis. The background spectra were obtained using blank-sky event lists (see Carter & Read 2007), filtered using the same procedures as for the source event lists. For each spectrum, response matrices and effective area files were produced, and for a good sampling of the PSF of the instrument, a region size of 12′ in radius was used.

The resulting spectra were merged using the SAS task *epicspeccombine* into a final background-subtracted source spectrum and then fitted using XSPEC 12 (Arnaud 1996). Due to a limited resolution of *XMM-Newton*, it was impossible to extract the spectra in close vicinity to a central source. Therefore, for the spectral analysis of the emission from the galactic core regions we used a model consisting of a gaseous component represented by a *mekal* model (Mewe et al. 1985; Kaastra 1992) and a power-law model (absorbed, if needed) to account for the emission of the hot gas and the central source (s), respectively. Finally, in two galaxies, NGC 4388 and NGC 4666, where the iron Fe–Kα line was clearly visible in the extracted spectrum, the power-law component was accompanied by a simple Gaussian to fit this line.

As we are interested in supplementary evidence for AGNs in the CHANG-ES sample, we focus only on those galaxies that show evidence for an AGN from the *XMM-Newton* data, of which there are eight galaxies. Observational details for these galaxies are presented in Table 3, the fitted models are in Table 4, and the derived photon indices and luminosities of the central sources in given in Table 5. Note that all fluxes and luminosities derived from X-ray spectra refer to the energy range 0.3–12 keV. A more thorough analysis of *XMM-Newton* data will be presented in a separate paper. Other examples of *XMM-Newton* analyses for the galaxies NGC 4666 and NGC 4013 can be found in Stein et al. (2019a) and Stein et al. (2019b).

[18] Twenty-four galaxies were observed, but good spectra could not be extracted for five of them.

Table 3
XMM-Newton X-Ray Observations of the Selected Galaxies

Galaxy	ObsID	Obs. Date	Column Density N_H[a]	Total/Clean[b] MOS Time[c] (ks)	Total/Clean pn Time (ks)
NGC 660	0093641001	2001 Jan 7	4.64	22/22	7/7
	0671430101	2011 Jul 18		37/3	n/a
NGC 2613	0149160101	2003 Apr 23	6.01	19/8	12/1
	0149160201	2003 May 20		59/54	28/22
NGC 2683	0671430201	2011 May 5	2.51	42/22	22/6
NGC 2992	0147920301	2003 May 19	4.87	55/47	26/22
NGC 3079	0110930201	2001 Apr 13	0.89	49/21	20/5
	0147760101	2003 Oct 14		82/66	39/14
NGC 3628	0110980101	2000 Nov 27	1.97	109/98	50/30
	0306060301	2005 Nov 15		34/34	15/14
NGC 4388	0110930701	2002 Dec 12	2.58	23/23	8/7
NGC 4594	0084030101	2001 Dec 28	3.70	85/85	n/a
NGC 4666	0110980201	2002 Jun 27	1.73	116/116	54/54
NGC 4845	0658400601	2011 Jan 22	1.44	42/41	19/12

Notes. See Section 2.2.
[a] Column density in (10^{20} cm^{-2}) weighted average value after LAB Survey of Galactic H I (Kalberla et al. 2005).
[b] Filtered for high background radiation.
[c] MOS1+MOS2.

3. Images and Data Products

For the BL data release, we have regridded all images to the same pixel size (0.5 arcsec^2) and trimmed to the same field size: 2000 × 2000 pixels, or 16.′7 on a side. A detailed description of these data products is given in Appendix B, and the panels are presented in Figure 1 and its online figure set. An explanation is provided below.

Table 4
Model Type and Reduced χ^2_{red}

Galaxy	Model	χ^2_{red}
NGC 660	wabs(mekal+wabs*powerlaw)	1.19
NGC 2613	wabs(mekal+powerlaw+wabs*powerlaw)	1.13
NGC 2683	wabs(powerlaw+wabs*powerlaw)	1.57
NGC 2992	wabs(powerlaw+wabs*powerlaw)	1.21
NGC 3079	wabs(mekal+mekal+powerlaw)	1.40
NGC 3628	wabs(mekal+wabs*powerlaw)	1.16
NGC 4388	wabs(mekal+powerlaw+wabs(powerlaw+Gauss))	1.31
NGC 4594	wabs*wabs*powerlaw	0.94
NGC 4666	wabs(mekal+mekal+wabs(powerlaw+Gauss))	1.35
NGC 4845	wabs*wabs*powerlaw	1.23

Note. Models: *wabs*—a photoelectric absorption using Wisconsin (Morrison & McCammon 1983) cross sections; *mekal*—emission from the hot gas, based on the calculation of Mewe et al. (1985) and Kaastra (1992); *powerlaw*—a simple photon power-law model.

Table 5
Photon Indices and Luminosities of the Central Sources in the Studied Galaxies

Region	Photon Index[a]	Luminosity (10^{40} erg s^{-1})
NGC 660	$2.45^{+0.81}_{-0.63}$	$0.47^{+1.09}_{-0.20}$
NGC 2613	$1.89^{+1.71}_{-0.86}$	$1.84^{+347}_{-1.73}$
NGC 2683	$1.69^{+1.05}_{-0.92}$	$0.92^{+27.5}_{-0.83}$
NGC 2992	1.66 ± 0.05	$764^{+57.6}_{-50.8}$
NGC 3079	$1.46^{+0.10}_{-0.12}$	$0.88^{+0.26}_{-0.19}$
NGC 3628	$1.46^{+0.07}_{-0.06}$	$0.73^{+0.13}_{-0.11}$
NGC 4388	$1.41^{+0.12}_{-0.11}$	$230^{+111}_{-72.8}$
NGC 4594	1.76 ± 0.05	$3.26^{+0.36}_{-0.31}$
NGC 4666	$1.77^{+0.17}_{-0.16}$	$2.55^{+1.23}_{-0.99}$
NGC 4845	2.09 ± 0.03	$539^{+39.2}_{-35.9}$

Note.
[a] Energy spectral index of photon counts (0.3–12 keV).

3.1. Noise Measurements

The rms noise values, measured prior to PB correction, are given in Table 2. The rms values show some variation with position on the image, depending on the locations and strengths of the sources in the field. For consistency between maps and also consistent with the approach taken in Wiegert et al. (2015), we quote rms values in Table 2 that are far from the center. Because most sources are quite weak in B configuration, residual sidelobes from cleaning were usually not excessive and the quoted rms noise variations over the map were typically $\lesssim$10%.

Exceptions are also present, though. For example, sources whose peak brightness exceeded 70 mJy beam^{-1} contained some residual sidelobes that remained after cleaning. Sources that were near other bright background sources in the sky, or sources in more crowded fields in general, had rms noise values that were larger closer to the target galaxy than in regions more distant from the center. Sources that fell into these categories have their rms values followed by an approximate factor by which the rms increases near the source itself.

Finally, the sources sometimes are found in a "negative bowl," which is expected when broad scale flux is missing ($>2'$ in L band at B configuration), as is the case for many of our galaxies.

Aside from the above-mentioned variations, the rms noise values on maps have been listed with an accuracy that reflects measurements on the maps themselves. Stokes Q and U maps, for example, show rms noise values that are very "clean" with little relative variation from location to location on any given map. In such cases, it is possible to measure the rms to a fraction of a μJy beam^{-1}. The reader is reminded, however, that the absolute flux calibration scale at the VLA for the primary calibrator, 3C 286, is $\approx$1% (Perley & Butler 2013). Individuals who download the images may wish to make their own measurements according to their scientific goals.

3.2. Total Intensity Images

The total intensity images (Stokes I) are shown in panels in the first row of Figure 1 and its online figure set. The corresponding rms values and peak brightnesses (I_{max}) are given in Table 2. Note that the peak value on a map could occur in an off-galaxy background source, so measurements of I_{max} were restricted to the region of the galaxy itself.

At the high resolution achieved for B configuration, though, and given the fact that steep-spectrum background sources will usually be brighter at L band than at C band, it is entirely possible that a discrete source seen in the region of the disk of a galaxy could in fact be a background source. We explore this possibility further in Section 6.2.

In several cases, *uv*-tapered images were not included because of poorer image quality; generally this was because of residual sidelobes either from the source itself or from an interfering background source.

3.3. Linear Polarization Images

In almost all cases, the linearly polarized images are nothing more than noise maps. As with the total intensity images, we measured the peak polarization, P_{max}, from the PB-corrected maps in the region of the galaxy itself. A scan down this column of Table 2 shows that almost every galaxy displays *no* emission above $5\sigma_{Q,U}$. Those galaxies that show higher values of P_{max} have comments in the last column as discussed next.

If there is emission above $5\sigma_{Q,U}$ but the peak values for rob 0 and *uv*-tapered images are at different locations, then they are labeled as "noise peaks," such as is the case for NGC 4244. For this galaxy, these peaks are unresolved points and have the appearance of random noise. The total intensity values at these peaks also show only noise.

If there is emission above $5\sigma_{Q,U}$ in one *uv* weighting but below $5\sigma_{Q,U}$ in the other weighting, then the emission is also not considered to be real. Such is the case for NGC 3735.

If higher emission is seen at both weightings, we then calculate the ratio, P_{max}/I (%), at the location of P_{max}. Since the polarization calibration is not considered to be reliable below about 0.5% (Irwin et al. 2015), signals that fall below this limit are also not considered to be real. This is the case for NGC 660 and NGC 4845, for example.

We are finally left with only two galaxies that could have real linearly polarized BL emission, these being NGC 3079 and NGC 4438, both of which are displayed in Figure 2. These galaxies are known to have strong nuclear activity.

In summary, given how little believable linear polarization is seen in the BL data, we do not release any polarization images. By contrast, the matching resolution CC data show quite

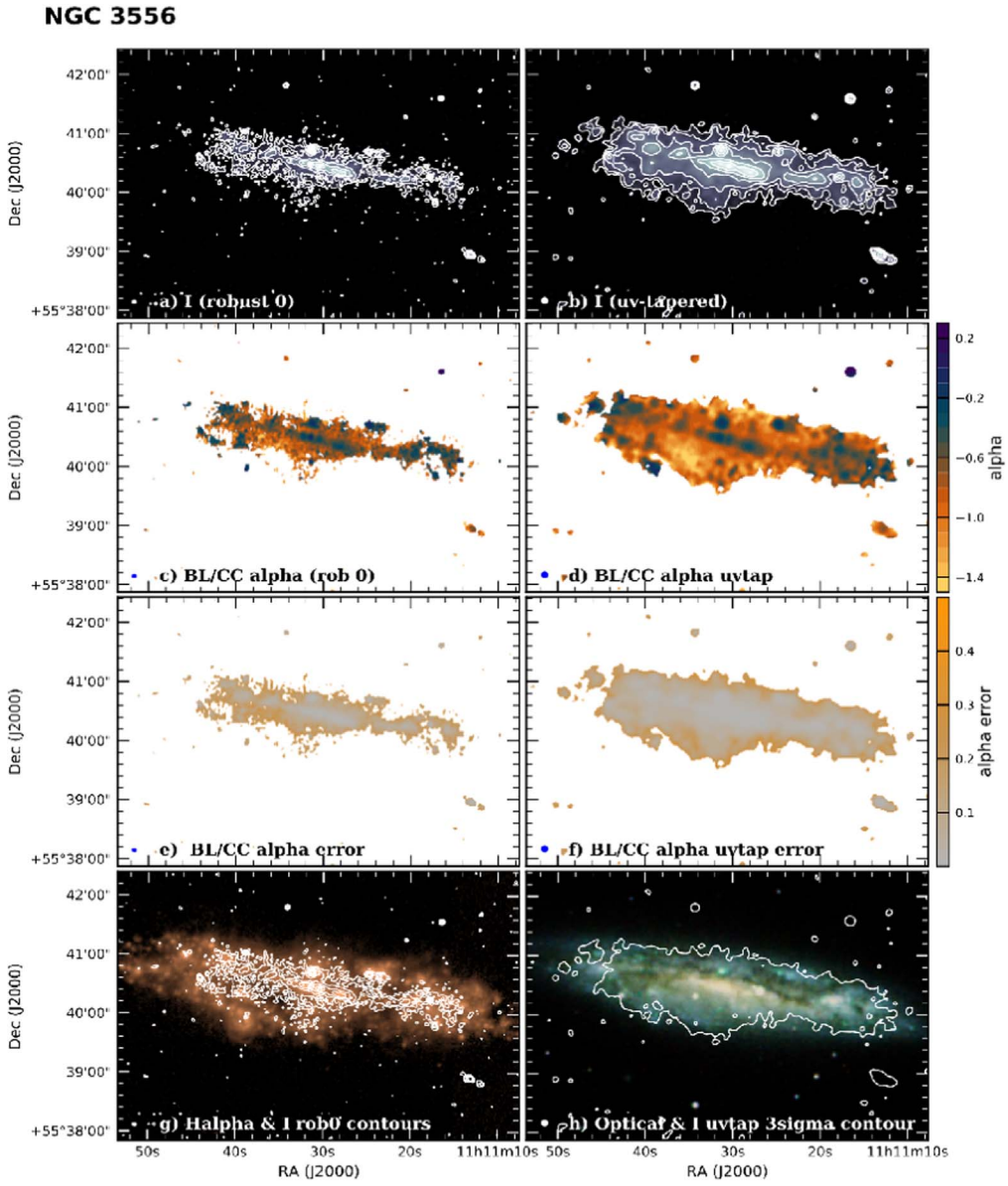

Figure 1. Panels for NGC 3556. A detailed description of these panels is given in Section 3 and Appendix B. The complete figure set (38 images) is available in the online journal.

(The complete figure set (38 images) is available).

significant polarization for most galaxies (R. Walterbos et al. 2019, in preparation), so it is clear that the lower-frequency *L*-band emission suffers from Faraday depolarization. It is possible that some *L*-band linear polarization could be reclaimed via a rotation measure synthesis analysis (e.g., Damas-Segovia et al. 2016). Further such analysis is, however, beyond the scope of the current paper.

3.4. BL to CC (Band-to-band) Spectral Index Maps

Spectral indices, α, are defined according to

$$I_\nu \propto \nu^\alpha. \quad (3)$$

Because of the weakness of most of the sources in B configuration, *in-band* spectral indices were noisier than desired for most galaxies. An example of a BL in-band spectral index map for one of our stronger sources, however, can be seen in Irwin et al. (2015).

We therefore made *band-to-band* spectral index maps from the BL central frequency of $\nu_L = 1.58$ GHz to the similar resolution CC central frequency of $\nu_C = 6.00$ GHz (the latter data have a 2 GHz bandwidth). The resulting spectral index maps (α maps) have a higher signal-to-noise ratio (S/N), but no variation in α between the bands can be recovered, should such variations be present.

Although the BL and CC data sets were very close in resolution and pixel size, some minor processing was required. The non-PB-corrected images were first regridded so that both had the same (smaller) pixel size. Then minor smoothing ($<2''$) was carried out so that the two images had exactly the same (larger) spatial resolution. New rms values (σ in the following discussion) were then measured for the BL and CC data sets. These rms values and adjusted beam sizes are listed in Table 6.

This process was then repeated for the PB-corrected images from which the spectral index maps were actually made. A 3σ

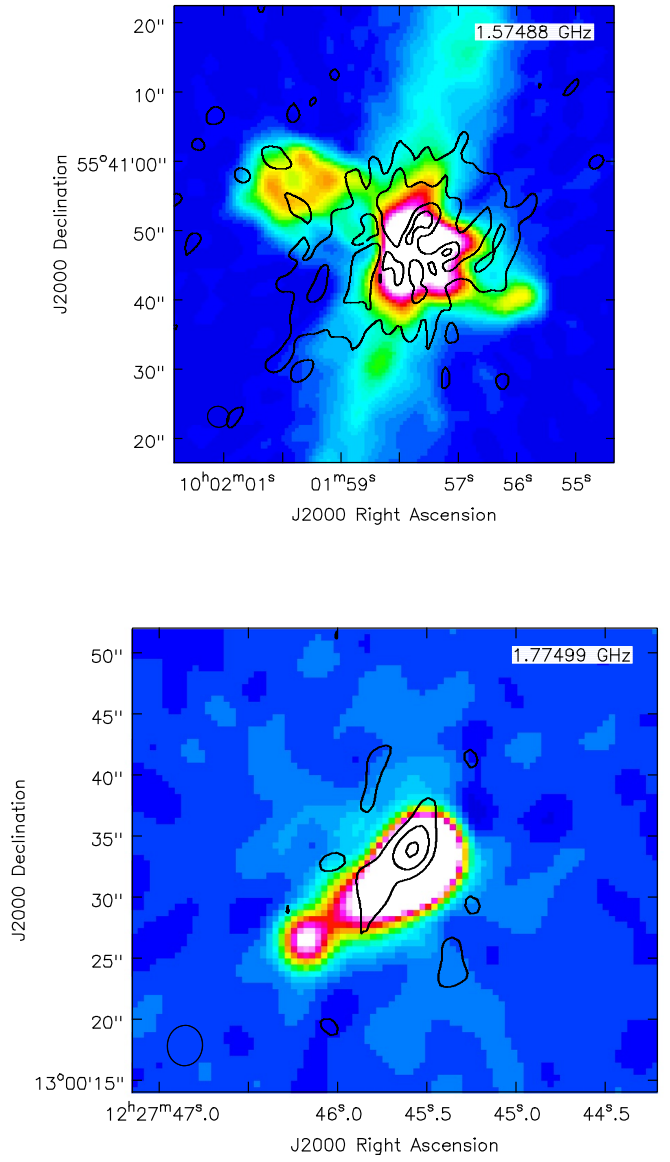

Figure 2. *L*-band rob 0 linear polarization (contours) over the total intensity image (color). The synthesized beam is shown as a black circle in the lower left corner, and frequency is given in the upper right corner. (a) NGC 3079. Contours are at 3, 7, and 15 $\times \sigma_{Q,U}$ ($\sigma_{Q,U} = 24.6$ μJy beam^{-1}; Table 2). The major axis extends NW to SE. (b) NGC 4438. Contours are at 3, 5, and 7 $\times \sigma_{Q,U}$ ($\sigma_{Q,U} = 41.6$ μJy beam^{-1}; Table 2).

cutoff was then applied to each of the BL and CC images prior to making band-to-band spectral index maps. This cutoff was adopted because tests showed that a higher 5σ cutoff removed some real features. Moreover, since noise peaks higher than 3σ are usually in different locations at the two frequencies, the 3σ cutoff produced the best results.

It should be pointed out that there are still artifacts in a few spectral index maps. This is because PB-corrected images have increasing noise with distance from the map center and some residual sidelobes remained for sources with strong emission. Examples are NGC 660 and NGC 3079, shown in the online figure set of Figure 1.

The final band-to-band spectral index maps shown in the second row of Figure 1 (and its online figure set) apply from 1.6 to 6.0 GHz.

3.4.1. Uncertainties in Spectral Index Maps

Spectral index error maps were formed using

$$\sigma_\alpha = \frac{1}{\ln\left(\frac{\nu_L}{\nu_C}\right)}\sqrt{\left(\frac{\sigma_L}{I_L}\right)^2 + \left(\frac{\sigma_C}{I_C}\right)^2}, \quad (4)$$

where the subscripts refer to the band and I represents the specific intensity at a given location. Note that since the rms values are measured from the maps, they include thermal noise, as well as any residual sidelobes that extend throughout the map. Uncertainties due to the deconvolution itself, as is the case for any imaging process, are typically not included.

Although the α maps have correctly taken the PB response at the two frequencies into account, the α-error maps, as given in Equation (4), have not. If higher accuracy is desired for σ_α, then the increasing noise with distance from the map center can be accounted for by multiplying the error maps by a position-dependent factor, $f(r)$, as given in Equation (11) of Appendix A.

To estimate the maximum correction factor that is required in our BL–CC α-error maps, we examine our largest angular-size spectral index map, which is the *uv*-tapered α map of NGC 5907 in Figure 1 (and its online figure set). At the farthest NW edge on the galaxy a distance at $r = 4\farcm5$ from the center, $\alpha \approx -0.3$, in which case $f(r) = 1.6$. The given error at this point from Equation (4) is $\sigma_\alpha \approx 0.3$, so the corrected error is $\sigma_{\alpha_{\rm corr}} = 0.46$. As can be seen from the error maps in the panels (panels (e) and (f)) and the sample calculation in Appendix A, typical corrections to the error maps are much lower than this.

3.4.2. Thermal Contribution to α_{BL-CC}

The band-to-band spectral index maps have not been corrected for possible contributions from thermal emission. Vargas et al. (2018) have done extensive work on estimating the spatially resolved thermal/nonthermal fraction in CHANG-ES galaxies at $\approx 15''$ resolution. To estimate the thermal contribution, these authors have used Hα maps that require a significant correction for extinction using additional 22 μm images. We do not pursue such a correction for our BL or CC images since appropriate infrared images are not available at equivalently high spatial resolution. At the centers of the galaxies (of particular interest for understanding AGN fractions), the adopted electron temperature (10^4 K) could also introduce some uncertainties in the thermal fractions.

A reasonable global estimate of an *L*-band thermal fraction is 8%, and that of a *C*-band thermal fraction is 20% (Vargas et al. 2018). Adopting these values, the nonthermal spectral index, $\alpha_{\rm BL-CC}$(NT), would be steeper than the observed spectral index, $\alpha_{\rm BL-CC}$, by only 0.1.

In the following discussion, then, we interpret our B configuration *L*-band data to be globally dominated by nonthermal emission, and this conclusion is confirmed by surveying the spectral index values shown in Figure 1 (see color scales), which are, on average, all steeper than $\alpha_{\rm TH} = -0.1$ (the value expected for thermal emission alone). The galaxy with the flattest spectral index averaged globally, NGC 4594 ($\overline{\alpha_{\rm BL-CC}} = -0.20 \pm 0.12$), whose value is numerically consistent with thermal emission, is straightforwardly explained by nonthermal emission from a central compact AGN (Section 5.3).

Table 6
Smoothed BL and CC Map Parameters as Input for Band-to-band Spectral Index Maps

Galaxy	Robust 0 Maps					*uv*-tapered Maps				
	BL rms (μJy beam^{-1})	CC rms (μJy beam^{-1})	bmaj (arcsec)	bmin (arcsec)	bpa (deg)	BL rms (μJy beam^{-1})	CC rms (μJy beam^{-1})	bmaj (arcsec)	bmin (arcsec)	bpa (deg)
NGC 660	20.6	3.85	4.0	3.5	−5	28.6	5.06	6.8	6.2	10
NGC 891	16.2	2.81	3.8	3.3	70	19.5	3.61	6.2	6.0	60
NGC 2613	18.1	32.3	7.5	5.5	−100	19.3	3.56	7.6	6.6	−7
NGC 2683	14.1	4.64	3.4	3.3	13	17.7	5.62	6.5	6.3	12
NGC 2820	15.6	2.58	3.6	3.5	21	17.5	2.97	6.3	6.3	56
NGC 2992	16.3	3.16	5.3	3.9	4	17.0	3.73	6.9	6.6	−40
NGC 3003	13.9	15.2	3.8	3.4	0	15.8	2.87	6.3	6.25	0
NGC 3044	15.5	3.57	4.1	3.9	15	18.1	4.34	7.5	6.6	3
NGC 3079	18.7	2.73	3.9	3.8	−15	30.0	3.73	6.8	6.4	−12
NGC 3432	20.7	2.97	3.4	3.4	2	22.6	4.45	6.5	6.3	−5
NGC 3448	15.5	2.57	3.7	3.5	62	17.5	3.06	6.1	6.0	1
NGC 3556	15.8	2.62	3.5	3.3	49	16.8	3.03	6.1	6.0	0.5
NGC 3628	14.6	4.28	4.2	3.8	−37	21.9	5.80	6.8	6.4	45
NGC 3735	15.7	2.49	3.6	3.5	29	18.8	3.64	6.5	6.4	−16
NGC 3877	10.3	2.79	3.6	3.3	−27	11.6	3.44	6.5	6.4	67
NGC 4013	13.7	2.39	3.6	3.3	−85	18.1	2.97	6.4	6.2	11
NGC 4096	14.3	2.83	3.4	3.3	−80	16.1	3.07	6.4	6.3	80
NGC 4157	11.1	2.88	3.3	3.1	−27	11.8	3.44	6.4	6.3	−20
NGC 4192	14.3	3.01	3.5	3.3	−37	19.7	3.75	6.4	6.1	84
NGC 4217	14.0	2.65	3.4	3.2	−82	15.6	3.06	6.2	6.1	0
NGC 4244	13.7	2.41	3.4	3.3	−18	15.3	2.56	6.3	6.2	20
NGC 4302	13.2	2.96	3.9	3.7	−38					
NGC 4388	17.6	2.93	4.0	3.7	−6					
NGC 4438	378	29.1	3.6	3.4	−4					
NGC 4565	14.6	2.62	3.6	3.3	−9	14.7	3.88	6.3	6.0	61
NGC 4594	17.0	2.69	4.8	3.7	−9	21.3	63.8	6.5	6.4	34
NGC 4631	16.0	2.77	3.7	3.5	−7					
NGC 4666	16.9	3.38	4.1	3.8	7					
NGC 4845	19.2	3.64	3.8	3.6	6					
NGC 5084	17.0	2.34	5.9	3.3	−8	18.2	2.78	7.8	6.8	39
NGC 5297	14.1	2.60	3.4	3.3	−10	16.7	2.83	6.3	6.2	−2
NGC 5775	13.4	2.80	4.0	3.8	29					
NGC 5792	14.7	2.89	4.2	3.8	21	16.1	3.83	7.5	6.7	−3
NGC 5907	12.2	2.53	3.7	3.2	40	11.8	3.58	6.3	6.2	−37
UGC 10288	13.5	2.88	4.2	3.9	28					

Note. The matching beams for BL and CC are designated "bmaj," "bmin," and "bpa" for the FWHM of the major axis, the FWHM of the minor axis, and the position angle, respectively.

Since the B configuration data have such high resolution, however, there could be discrete regions in the disk, specifically H II region complexes, for which the thermal fraction departs from this general result. We provide one example in Section 6.1.

4. The Images and High-resolution Structures

The first row of the panels in Figure 1 (and its online figure set) show a wide variety of emission in these high-resolution images. In total intensity, we see compact cores of varying strength (e.g., NGC 2613, NGC 4845, and others), numerous compact regions in the disk—likely H II region complexes (e.g., NGC 3432, NGC 4244, and others)—and vertical diffuse emission away from the plane (e.g., NGC 3044, NGC 4666, and again others).

Particularly interesting is the complex structure that can be seen in many spectral index maps (second row) that may be masked in the total intensity images. The fact that more structure/information can be available from spectral index maps than from total intensity maps has been noted in the past (e.g., Lee et al. 2001), but several remarkable examples are seen in the CHANG-ES sample.

An example is NGC 3448 (Figure 3 top). In the spectral index map (colors) we see evidence for a spiral arm curving from R.A. $\approx 10^{h}54^{m}38^{s}$, decl. $\approx 54^{h}18^{m}23^{s}$ to R.A. $\approx 10^{h}54^{m}39^{s}$, decl. $\approx 54^{h}18^{m}33^{s}$. The arm is delineated by three spectral index peaks that are somewhat flatter than their surroundings (≈ -0.53) and typical of multiple young supernova remnants (SNRs). Yet no such structure is visible in the *L*-band total intensity image alone. Only three contours are shown in Figure 3, but an inspection of the image as a whole (see the NGC 3448 image in the online figure set of Figure 1) shows no such feature. The *C*-band image structure (R. Walterbos et al. 2019, in preparation) of course will differ from the *L*-band image, hence leading to the structure in spectral index, but such a feature is again not obvious at all at *C* band. It is really the spectral index map that clearly reveals this structure, otherwise masked in total intensity. A possible arm may also be present on the opposite side of the nucleus centered at R.A. $\approx 10^{h}54^{m}41^{s}$, decl. $\approx 54^{h}18^{m}20^{s}$.

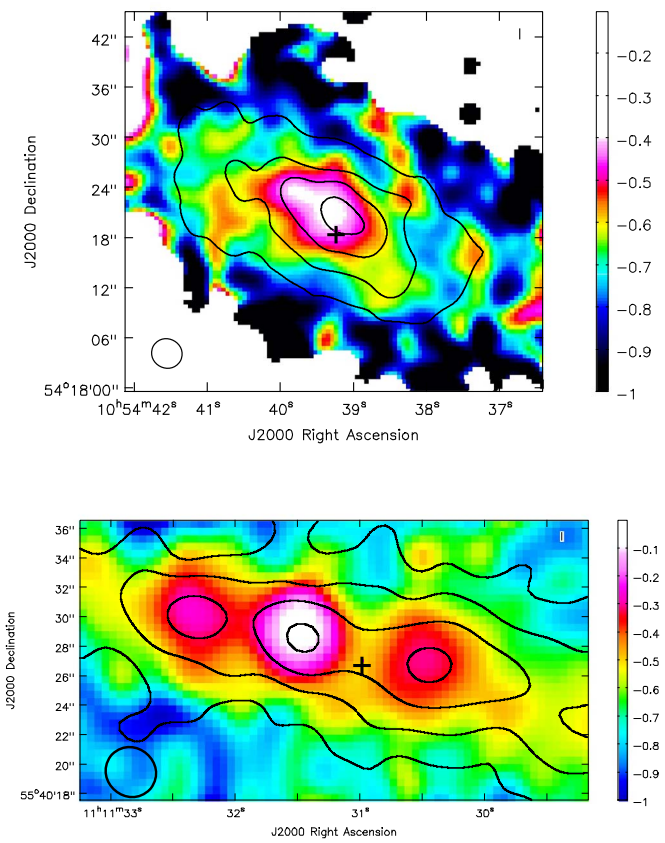

Figure 3. *L*-band total intensity contours for the rob 0 weighting images over spectral index image with color scale shown at right. The beam of the spectral index image is shown at lower left. (a) NGC 3448. Contours are at 170 ($10\sigma_I$), 400, 800, and 2000 μJy beam^{-1}. The NED galaxy center is marked with a plus sign. (b) NGC 3556. Contours are at 160 ($10\sigma_I$), 300, 600, and 1500 μJy beam^{-1}. The NED galaxy center is marked with a plus sign.

Another example is NGC 3556 (Figure 3, bottom) which shows three distinct peaks in the spectral index map that are present, but not so strongly obvious, in the total intensity image. The peaks are suggestive of radio lobes. For example, if the white, flattest spectral index peak actually represents the galaxy center (offset from the NED center that is marked with a plus sign), then it is possible that the two other peaks on either side of it represent young radio lobes a distance ≈530 pc from the center. However, since these features are in the disk in projection, it is possible that they are instead associated with other in-disk features, such as edge-on spiral arms or rings.

We provide another remarkable example in Section 5.1.3.

5. AGNs in the CHANG-ES Sample

The fact that radio emission does not suffer from extinction is a strong incentive for using our high-resolution BL images for determining whether or not an AGN is present. For edge-on galaxies, such incentive is even stronger.

In the past, it has been difficult to disentangle AGNs from nuclear starbursts in spiral galaxies. The search for weak or hidden AGNs has been of particular interest, especially given the possibility that lower-mass AGNs in galaxy nuclei could be on the same fundamental plane (i.e., the plane of black hole accretion relating radio emission, X-ray emission, and mass of an accreting black hole) as supermassive black holes and stellar-mass black holes (e.g., Gültekin et al. 2014).

It has long been recognized that excessive luminosities within galaxy nuclei can indicate the presence of an AGN (e.g., Section 5.1.2). However, "dwarf" AGNs, or "low-luminosity AGNs" (LLAGNs), i.e., those with Hα luminosities lower than 10^{40} erg s^{-1} (Ho et al. 1997) or with X-ray luminosities below 10^{42} erg s^{-1} (Ho 2009), may also be present yet hidden among other camouflaging emission.

In the CHANG-ES sample, there is already previous evidence for the presence of many AGNs or LLAGNs, for example, a Seyfert (Sy) categorization, or the presence of a low-ionization nuclear emission region (LINER) for LLAGNs (Maoz 2008). We identify these via their NED (NASA/IPAC Extragalactic Database) type, which we list in Table 10. A study by Nagar et al. (2005) also identified ≈200 LLAGNs within which eight CHANG-ES galaxies appear, although they do not reveal any new LLAGNs other than those already identified in Table 10.

5.1. Radio Criteria for Determining the Presence of an AGN

Our goal is to determine criteria for an AGN from the radio emission alone and then compare our results to what has been previously known. In addition, we supplement our data with X-ray data for a subset of the galaxies (Section 2.2).

Radio criteria that provide evidence of an AGN are as follows: (1) the presence of an unresolved point-like core, (2) a luminosity that is too high to be accounted for from a collection of SNe alone, (3) the presence of radio jets or lobes, (4) the presence of a relatively flat or positive spectral index at the nucleus, (5) a brightness temperature T_B that is too high to be accounted for by thermal gas, (6) variability, and (7) the presence of circular polarization. We will consider each of these in turn.

Our brightest source is NGC 660, which has a peak specific intensity of 245 mJy beam^{-1} at the highest resolution. This corresponds to a brightness temperature of $T_B \approx 10^4$ K, which does not put meaningful constraints on this value; in other words, the beam size is too large for any embedded AGN to distinguish itself, should it have a high brightness temperature (Point 5).

Variability (Point 6) is a clear indicator of an AGN. Even a weak AGN, such as the LLAGN at the Galactic center, is variable on timescales of weeks to months (Contini 2011), and CHANG-ES data sets are separated by months (e.g., Table 1). We do find variability of a central AGN by careful comparison and fitting of the central source brightness over all CHANG-ES data sets for the galaxy, NGC 4845 (Irwin et al. 2015). However, this source was rather extraordinary, displaying a tidal disruption event (TDE). For the remaining galaxies, a comparison was made between the flux densities of the B configuration *L*-band images and the C configuration *L*-band images (the former smoothed to the resolution of the latter), but no convincing variability was found beyond minor differences that could be attributed to differences in *uv* coverage. Similar analysis to NGC 4845, which will be feasible only for the stronger sources, is beyond the scope of this paper.

Circular polarization in the cores of the galaxies (Point 7) has been examined thoroughly for the BL data in Irwin et al. (2018). This paper outlines the uncertainties involved in this process and adopts conservative criteria for concluding that circular polarization exists. The conclusion is that five galaxies show evidence for circular polarization, and these are indicated in Table 10.

Table 7
Galaxies with Point Cores

Galaxy	R.A.[a] (h m s)	Decl.[a] (° ′ ″)	S_ν[b] (mJy)	Avg. FWHM[c] (pc)	L_ν[d] (10^{19} W Hz^{-1})	No.$_{SNR}$[e]
NGC 660*	01 43 02.320	+13 38 44.88	296 ± 5	176	536	1786
NGC 2613	08 33 22.772	−22 58 24.81	0.37 ± 0.02	398	2.42	8
NGC 2683	08 52 41.31	+33 25 18.79	1.13 ± 0.03	81	0.531	2
NGC 3079	10 01 57.793	+55 40 47.27	152 ± 5	272	772	2572
NGC 3735	11 35 57.204	+70 32 07.77	1.9 ± 0.2	572	40.1	134
NGC 4388*	12 25 46.747	+12 39 41.69	31.5 ± 0.9	242	104	346
NGC 4438*	12 27 45.548	+13 00 32.98	57 ± 3	139	73.6	245
NGC 4565	12 36 20.771	+25 59 15.68	1.57 ± 0.01	161	2.66	9
NGC 4594	12 39 59.433	−11 37 23.02	70.50 ± 0.06	205	136	453
NGC 4666*	12 45 08.632	−00 27 42.99	4.2 ± 0.2	430	38.0	127
NGC 4845*	12 58 01.196	+01 34 32.42	210.8 ± 0.6	250	727	2424
NGC 5084*	13 20 16.831	−21 49 38.29	30.4 ± 0.3	410	199	664
NGC 5297	13 46 23.673	+43 52 20.22	0.21 ± 0.02	530	4.10	14

Notes. Measured by doing Gaussian fitting of the cores of the rob 0 weighted maps. The fitted region was approximately twice the size of the beam FWHM. Asterisks denote galaxies whose positions differ from the NED centers.
[a] Fitted center of the core. Uncertainties are ≈0.″2 in both coordinates.
[b] Flux density of the fitted Gaussian component.
[c] Average linear size of the major and minor axes of the total intensity maps.
[d] Spectral power corresponding to the flux density of the Gaussian component.
[e] Number of average M82 SNRs ($\overline{L_\nu} = 3 \times 10^{18}$ W Hz^{-1}) corresponding to the measured spectral power, rounded to an integer.

This leaves us with Points 1 through 4, which will be explored below.

5.1.1. Point-like Cores

Table 7 lists the galaxies that have point-like cores. We determine this by fitting a Gaussian to the centers of each galaxy and listing only those galaxies for which the FWHM of the source, after deconvolving from the synthesized beam, is less than the synthesized beam FWHM in *both* the major- and minor-axis directions. This criterion picks out strong candidates for an LLAGN but allows for minor contributions from other emission components that may also be centrally concentrated.

Thirteen galaxies fall into this category. Of these galaxies, to our knowledge, five show a radio point core for the first time from the CHANG-ES sample. These galaxies are NGC 2613, NGC 4845 (Irwin et al. 2015), NGC 4666 (Stein et al. 2019a), NGC 5084, and NGC 5297. Moreover, for NGC 2613 the radio point core provides the first evidence for a possible AGN in any band (see also Desouza 2017).

The fitted positions of these cores are also listed in Table 7. We have compared these positions to the suggested position of the source centers in NED. Six of the 13 sources have positional differences greater than the error, with four of those sources having positional offsets greater than three times the error. These six galaxies are marked with an asterisk in Table 7. We argue that these radio core positions likely designate the true centers of these galaxies (except for NHGC 4438, see Section 5.1.3).

We stress that this criterion alone is not a definitive argument for an AGN. For example, it is possible that a starburst could be so compact in the nuclear region of the galaxy (sizes typically several hundred parsecs, Table 7) that a number of SNe might also appear point-like. Alternatively, a weak AGN could still be present but masked (and missed) if other broader-scale emission simply swamps that of an LLAGN. Higher-resolution data, e.g., Very Long Baseline Interferometry (VLBI) detections, should further reveal AGN activity (e.g., Nagar et al. 2005, and references therein).

5.1.2. Radio Luminosities

It is well known that an AGN could (but need not) have a high luminosity in comparison to a collection of SNRs from an SF region in a given area.

The best-known and well-studied extragalactic SF region is in the "starburst galaxy" M82, which shows ≈40 SNRs at 5 GHz (Muxlow et al. 1994) and 20 SNRs at 408 MHz (Wills et al. 1997) in a region ≈600 pc in diameter. The average spectral luminosity of the nuclear SNRs in M82 at 20 cm is $L_\nu = 3 \times 10^{18}$ W Hz^{-1} (data from Allen & Kronberg 1999), with a standard deviation of the same order of magnitude. The star formation rate (SFR) of M82 is 3.6 $M_\odot$ yr^{-1} (Grimm et al. 2003), which exceeds all but two values of the CHANG-ES sample (Wiegert et al. 2015).

Although such a comparison is not absolutely definitive, it is still useful to ask how many M82 mean SNRs could be accounted for by the measured luminosities in the cores of the galaxies of Table 7. The last column gives this result, and the fifth column gives the size of the region to which it applies. All galaxies except NGC 2613, NGC 2683, NGC4565, and NGC 5297 have luminosities that exceed what is seen in the starburst galaxy M82. This suggests that the remaining nine galaxies likely harbor relatively active AGNs, with NGC 3079 being the most powerful.

For the galaxies that do not have point-like cores (Table 8) or at least have a deconvolved Gaussian size that is wider than the synthesized beam in at least one direction, we repeat this exercise. From this list, NGC 2992 by far "outshines" all other galaxies. Here almost 9000 M82 mean SNRs would be required to reproduce the observed luminosity in a region that is about the same as the M82 nuclear starburst. From this result, NGC 2992 clearly has an AGN and, in fact, has been found to have polarized radio jets that have been explored in detail in Irwin et al. (2017).

Table 8
Galaxies without Point Cores

Galaxy	R.A.[a] (h m s)	Decl.[a] (° ′ ″)	S_ν[b] (mJy)	Avg. FWHM[c] (pc)	L_ν[d] (10^{19} W Hz^{-1})	No.$_{SNR}$[e]
NGC 891	02 22 33.22	+42 20 57.6	10.2 ± 0.6	132	10.0	33
NGC 2820	09 21 45.97	+64 15 28.0	3.1 ± 0.2	733	26.9	90
NGC 2992	09 45 41.95	−14 19 35.8	195 ± 5	650	2700	8990
NGC 3003	09 48 35.68	+33 25 17.9	1.08 ± 0.04	300	8.34	28
NGC 3044	09 53 40.87	+01 34 46.7	4.1 ± 0.2	263	20.2	67
NGC 3432	10 52 30.94	+36 37 08.2	0.80 ± 0.09	239	0.85	3
NGC 3448	10 54 39.17	+54 18 20.5	6.8 ± 0.3	441	48.8	163
NGC 3556[f]	…	…	…	…	…	…
NGC 3628	11 20 16.99	+13 35 20.2	175 ± 4	115	150	501
NGC 3877	11 46 07.71	+47 29 40.0	2.4 ± 0.1	204	9.03	30
NGC 4013	11 58 31.38	+43 56 51.0	7.7 ± 0.4	192	23.6	79
NGC 4096	12 06 01.23	+47 28 41.5	0.16 ± 0.04	111	0.20	1
NGC 4157[f]	…	…	…	…	…	…
NGC 4192	12 13 48.28	+14 54 02.3	4.8 ± 0.7	155	10.5	35
NGC 4217	12 15 50.95	+47 05 29.2	4.1 ± 0.3	271	20.8	69
NGC 4244[g]	…	…	…	…	…	…
NGC 4302	12 21 42.31	+14 35 52.4	1.70 ± 0.04	212	7.64	25
NGC 4631	12 42 07.87	+32 32 34.9	7.3 ± 0.3	151	4.78	16
NGC 5775[h]	14 53 57.50	+03 32 41.3	7.7 ± 0.5	1078	76.9	256
NGC 5792[f]	…	…	…	…	…	…
NGC 5907[f]	…	…	…	…	…	…
UGC 10288	16 14 24.83	−00 12 27.7	0.19 ± 0.03	399	2.60	9

Notes. Measured by doing Gaussian fitting of the highest total intensity peak at or closest to the cores of the rob 0 weighted maps. The fitted region was approximately twice the size of the beam FWHM.
[a] Fitted center of the core. Uncertainties are ≈0.″2 in both coordinates.
[b] Flux density of the fitted Gaussian component.
[c] Average linear size of the major and minor axes of the Gaussian fit, after deconvolving from the synthesized beam.
[d] Spectral power corresponding to the flux density of the Gaussian component.
[e] Number of average M82 SNRs ($\overline{L_\nu} = 3 \times 10^{18}$ W Hz^{-1}).
[f] No distinct peak at the core.
[g] Emission is too weak to measure.
[h] Peak is blended with extended emission to the NW.

A second galaxy that stands out is NGC 3628, requiring ≈500 SNe within 115 pc to explain its luminosity. This galaxy also has circularly polarized emission (Irwin et al. 2018) and radio lobes (next section).

5.1.3. Jets/Lobes

Determining whether a jet or lobe is present from radio data is somewhat more subjective than the previous criteria since it relies on morphology; such structures may be embedded in other emission, especially since these features might not (yet) have emerged from the disk. Here, if we see bipolar structure, we interpret this as a jet or lobe. Such a result does not preclude the possibility of additional winds from starbursts, but a bipolar feature seen in nonthermal radio emission is most likely explained by an AGN. In the following, we refer to such structures as lobes, rather than jets, since our spatial resolution is insufficient to detect narrow jets that would be connected to the nucleus.

Several galaxies show clear radio lobes that have previously been known. Examples are NGC 4388 (e.g., Hummerl & Saikia 1991; Damas-Segovia et al. 2016, among others) and NGC 3079 (Hummel et al. 1984, among others), and these are also seen in the panels of Figure 1 and its online figure set. Figure 8 of Irwin et al. (2017) also reveals how the lobes in NGC 3079 are more distinctly seen in linear polarization compared to total intensity.

In Figure 4 (top), we show a CHANG-ES example of a previously known radio lobe, i.e., the inner region of NGC 4438, with total intensity contours revealing the NW −SE outflow direction. The spectral index, moreover, also clearly reveals the same structure. The mean spectral index within the 1 mJy beam^{-1} total intensity contour (second contour) is $\alpha_{BL-CC} = -0.757 \pm 0.005$. This is an example of a steep spectrum that is typically observed for radio lobes. The position of the core from higher spatial resolution radio images suggests that its likely location is near the NED center marked in the figure (J2000: $12^h27^m45\overset{s}{.}67$, $+13^d00^m31\overset{s}{.}54$; Hota et al. 2007). The core is presumably a flatter spectrum source whose emission is too weak to perturb the spectral index of the lobe, as seen in the image.

A new and very interesting result, however, is that radio lobes could be revealed *only* in the spectral index (hidden lobes) and *not* in the total intensity image; again, the weak lobes are masked by other sources of emission in total intensity as previously described in Section 4. Presumably, the spectral index map *can* reveal the radio lobes because the energy spectral dependence of cosmic-ray electrons will be different in the outflow than in the surrounding regions.

A good example of this is in NGC 3628 (Figure 4, middle). Here we see the total intensity emission (contours) smoothly increasing to a peak at the center of the galaxy. Above and below the nucleus are two regions of relatively flat spectral index, ≈−0.34 for the south peak (Table 9) and ≈−0.43 for the

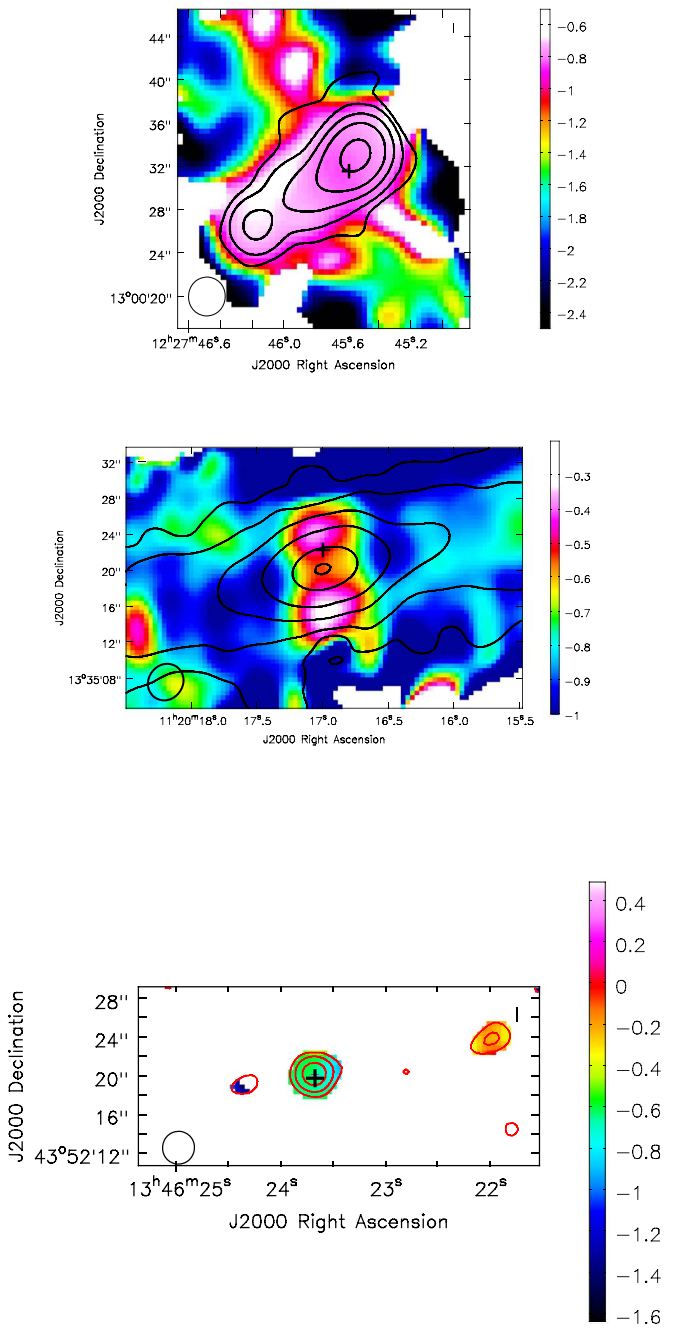

Figure 4. Total intensity contours for the rob 0 weighting images over spectral index image with color scale shown at right. The beam of the spectral index image is shown in the lower left corner, and the NED center of the galaxy is marked with a plus sign. Top: NGC 4438. Contours are at 400 ($10\sigma_I$), 1000, 3000, 8000, and 25,000 μJy beam^{-1}. Middle: NGC 3628. Contours are at 232 ($10\sigma_I$), 500, 1500, 5000, 30,000, and 75,000 μJy beam^{-1}. Bottom: NGC 5297. Contours are at 40.8 ($3\sigma_I$), 65, and 100 μJy beam^{-1}.

north peak. The center of the galaxy must be located at the position of the total intensity radio continuum peak, i.e., R.A. = $11^h20^m17\overset{s}{.}01$, decl. = $13^h35^m20\overset{s}{.}1$. This center is $2\overset{''}{.}6$ below the NED peak, which is marked with a plus sign in the figure. The NED position was adopted from *Chandra* X-ray data (Evans et al. 2010). Notice that the spectral index is flatter than that of the radio outflow for NGC 4438. This suggests that the outflow in NGC 3628 could be young in comparison.

In Table 10 we list galaxies that appear to show radio lobes. The two galaxies with question marks are NGC 3556, which has three peaks along the disk in both total intensity and spectral index (Figure 3, bottom), and NGC 5297 (Figure 4, bottom), which has two very weak features on either side of the nucleus, the westernmost "lobe" having a spectral index of −0.23.

In summary, we have searched through the BL data for evidence of new radio lobes (beyond what has been previously known) and find evidence for lobes in NGC 3628, and possibly NGC 3556 and NGC 5297; these features are revealed in the *spectral index* maps, rather than total intensity.

5.1.4. "Flat" Spectral Indices in Nuclei

With nonthermal emission dominating (Section 3.4.2), we expect flatter spectral indices for AGNs as opposed to a group of SNRs. It is well known, for example, that AGNs can have very flat and sometimes positive spectra owing to the fact that AGNs are compact, can consist of multiple components, and can show self-absorbed synchrotron spectra.

As pointed out in the previous section (e.g., NGC 4438), the core of an AGN could be blended with steeper spectrum outflows, so this criterion will only select a subset of AGNs. It is important, however, to ask whether a collection of SNRs (also nonthermal emission) at a galaxy's nucleus could produce a flat spectral index and masquerade as an AGN.

For SNRs the theoretical value derived from diffusive shock acceleration (DSA) is $\alpha = -0.5$, and 20% of all SNRs have measured values consistent with this value. Observationally, even young SNRs have steep spectral indices, typically of about −0.7 (Urošević 2014) prior to significant cosmic-ray electron (CRE) aging and spectral steepening. The youngest known SNR in our Galaxy (about 100 yr), for example, has a spectral index of −0.65 at 1 GHz (Reynolds et al. 2008). A sampling of Galactic and extragalactic SNRs by Bell et al. (2011) shows spectral indices ranging from −0.4 to −1.1.

So-called "flat-spectrum" SNRs have spectral indices in the range of $-0.2 > \alpha > -0.5$ (Urošević 2014). Theoretically, such flat spectral indices can occur intrinsically (e.g., see chap. 21 of Longair 1994, for second-order Fermi acceleration) and have been observed for individual SNRs in the Galaxy (Urošević 2014). A *collection of SNRs* in the nuclear region of a galaxy, however, is unlikely to show intrinsically flat spectral indices at *L* band.

Nonintrinsic flattening of the spectral index could occur from the presence of a strong thermal bremsstrahlung component. Thermal absorption is unlikely for a collection of SNRs at *L* band (Section 6.1), but flattening due to thermal emission (for which $I_\nu \propto \nu^{-0.1}$) is sometimes observed for individual Galactic SNRs when they are embedded in molecular clouds (Onić et al. 2012).

A good example of emission that is primarily from a sample of supernovae in the nuclear region of a galaxy is, again, M82. Various authors find low-frequency spectral turnovers in individual SNRs in M82 owing to thermal absorption, implying emission measures (EMs) of typically 10^6 cm^{-6} pc (Kronberg & Wilkinson 1975; Carlstrom & Kronberg 1991; Wills et al. 1997), consistent with radio recombination line EM results (Seaquist et al. 1985), although a few $\times 10^{7-8}$ cm^{-6} pc have also been cited from very high resolution observations (i.e., 1.6 pc; McDonald et al. 2002). However, the mean spectral index from this collection of SNRs is still quite steep, on average: -0.6 ± 0.2 (Wills et al. 1997) at 408 MHz and -0.4 ± 0.3 at 5 GHz (Kronberg & Sramek 1992), in a region

Table 9
Flattest Spectral Index Closest to the Galaxy's Center

Galaxy	R.A.[a] (h m s)	Decl.[a] (° ′ ″)	α_{BL-CC}[b]	Avg. FWHM[c] (pc)
NGC 660	01 43 02.33	+13 38 44.7	+0.527 ± 0.003	198
NGC 891	02 22 33.29	+42 20 57.9	−0.446 ± 0.002	138
NGC 2613[d]	08 33 22.76	−22 58 25.0	−0.102 ± 0.140	646
NGC 2683	08 52 41.31	+33 25 18.0	−0.070 ± 0.016	90.2
NGC 2820	09 21 46.04	+64 15 27.6	−0.450 ± 0.015	404
NGC 2992	09 45 41.89	−14 19 33.5	−0.653 ± 0.001	664
NGC 3003	09 48 35.62	+33 25 17.3	−0.363 ± 0.030	392
NGC 3044	09 53 40.78	+01 34 47.2	−0.448 ± 0.004	349
NGC 3079	10 01 57.86	+55 40 47.3	+0.116 ± 0.005	341
NGC 3432[e]	10 52 31.13	+36 37 07.6	−0.125 ± 0.110	138
NGC 3448	10 54 39.33	+54 18 21.90	−0.389 ± 0.005	379
NGC 3556	11 11 31.50	+55 40 29.3	−0.079 ± 0.008	206
NGC 3628	11 20 16.97	+13 35 15.4	−0.341 ± 0.003	146
NGC 3735	11 35 57.19	+70 32 08.1	−0.505 ± 0.006	641
NGC 3877[d]	11 46 07.69	+47 29 39.6	−0.342 ± 0.007	262
NGC 4013	11 58 31.38	+43 56 50.7	−0.515 ± 0.003	237
NGC 4096[e]	12 06 01.13	+47 28 42.4	−0.327 ± 0.083	149
NGC 4157	12 11 04.57	+50 29 03.3	−0.477 ± 0.031	214
NGC 4192[e]	12 13 48.29	+14 54 01.2	−0.663 ± 0.004	198
NGC 4217[d]	12 15 50.90	+47 05 29.3	−0.614 ± 0.006	292
NGC 4244[f]	…	…	…	…
NGC 4302[g]	12 21 41.99	+14 35 44.2	−0.345 ± 0.130	317
NGC 4388	12 25 46.68	+12 39 46.0	−0.158 ± 0.005	274
NGC 4438	12 27 46.11	+13 00 29.7	−0.674 ± 0.012	156
NGC 4565	12 36 20.9	+25 59 15.0	−0.527 ± 0.016	176
NGC 4594[d]	12 39 59.43	−11 37 23.0	+0.432 ± 0.005	230
NGC 4631	12 42 07.80	+32 32 34.9	−0.388 ± 0.020	114
NGC 4666[e]	12 45 08.59	−00 27 42.8	−0.672 ± 0.004	466
NGC 4845[d]	12 58 01.19	+01 34 32.5	+0.376 ± 0.005	270
NGC 5084[d]	13 20 16.83	−21 49 38.5	+0.077 ± 0.009	444
NGC 5297[d]	13 46 23.7	+43 52 20.5	−0.638 ± 0.100	581
NGC 5775[g]	14 53 57.57	+03 32 30.6	−0.487 ± 0.010	484
NGC 5792[e]	14 58 22.71	−01 05 27.9	−0.606 ± 0.003	544
NGC 5907[d]	15 15 53.50	+56 19 43.5	−0.624 ± 0.033	248
UGC 10288[f]	…	…	…	…

Notes. Measured from the rob 0 weighted maps.
[a] R.A. and decl. of the location of a flattest spectral index feature near the nucleus unless otherwise indicated. Note that this is not necessarily at the NED center of the galaxy or at the peak in total intensity (see Section 5.1.4).
[b] Mean spectral index within an FWHM (from Table 6). The error is the mean value from the related error map (Equation (4)) in the same region, or the variation that results from altering the position of the FWHM by approximately 1 pixel, whichever is larger. See Section 3.4.1 for further discussion of the errors.
[c] Linear size corresponding to the average of the major and minor axes (bmaj and bmin of Table 6) of the spectral index maps.
[d] Measured at the central total intensity peak.
[e] No distinct spectral index feature; measured at NED center.
[f] Too faint to measure.
[g] Peak of α_{BL-CC} is offset ≈10″ from the nucleus.

≈600 pc in diameter, which is similar in size (to order of magnitude) to the CHANG-ES galaxies (Tables 7 and 8). Between 74 MHz and 23 GHz, 19 out of 26 compact sources in M82 have $\alpha < -0.49$. For more up-to-date data on M82, see, e.g., Adebahr et al. (2013) and Varenius et al. (2015).

In summary, we would not expect a collection of SNRs in the nuclear region of an external galaxy to show a mean spectral index flatter than $\alpha \approx -0.3$ unless thermal emission from gas with extremely high EMs ($\gg 10^6$ cm^{-6} pc) is present throughout the region. We therefore adopt $\alpha \geqslant -0.3$ at the nucleus as evidence for an AGN.

In Table 9 we provide spectral index measurements near the nucleus of each CHANG-ES galaxy. Since the NED nucleus does not always indicate the true center of the galaxy (e.g., NGC 3628; Figure 4, middle), we make measurements at the location of the flattest spectral index that is closest to the NED center. These locations (R.A. and decl.) are specified in the table. Note also that not every galaxy shows a distinctly flatter spectral index anywhere near the nucleus; see notes to the table for further clarity. Measurements close to where the emission was cut off (blanked) were also avoided because of spurious spectral index values at the boundaries.

In Table 9, we also provide the linear size corresponding to the average beam size of the synthesized spectral index maps, as well as the number of SNRs that would have to be present in this region, should those SNRs have the average spectral power of the SNRs in the well-known starburst galaxy M82.

Using the flat spectral index criterion, we find that eight galaxies show evidence for AGNs. These are denoted in Table 10.

Table 10
AGN Candidates

Galaxy	NED Type[a]	*XMM-Newton*[b]	Flat α_{BL-CC}[c]	Point Core[d]	High L_ν[e]	Lobe(s)[f]	CP[g]	AGN[h]
NGC 660	SB(s)a pec; H II, LINER	N	Y	Y	Y	Y	Y	Y
NGC 891	SA(s)b? sp; H II	N						N
NGC 2613	SA(s)b; H II	Y	Y	Y				Y
NGC 2683	SA(rs)b; LINER, Sy2	Y	Y	Y				Y
NGC 2820	SB(s)c pec sp	⋯						N
NGC 2992	Sa pec; Sy1.9	Y			Y	Y		Y
NGC 3003	SBbc	⋯						Y
NGC 3044	SB(s)c? sp; H II	⋯						N
NGC 3079	SB(s)c; LINER, Sy2	N	Y	Y	Y	Y	Y	Y
NGC 3432	SB(s)m; LINER, H II	⋯	Y					Y
NGC 3448	I0	⋯						N
NGC 3556	SB(s)cd; H II	⋯	Y			Y?		Y
NGC 3628	SAb pec sp; H II, LINER	Y			Y	Y	Y	Y
NGC 3735	SAc: sp; Sy2	⋯		Y	Y			Y
NGC 3877	Sc; H II	⋯						N
NGC 4013	SAb; H II, LINER	N						N
NGC 4096	SAB(rs)c; H II	⋯						N
NGC 4157	SAB(s)b? sp; H II	N						N
NGC 4192	SAB(s)ab; H II, Sy, LINER	⋯						N
NGC 4217	SAb sp; H II	⋯						N
NGC 4244[i]	SA(s)cd: sp; H II	⋯	⋯	⋯	⋯	⋯	⋯	⋯
NGC 4302	Sc: sp; Sy,LINER	N						N
NGC 4388	SA(s)b: sp; Sy2, Sy1.9	Y	Y	Y	Y	Y	Y	Y
NGC 4438	SA(s)0/a pec:; LINER	N		Y	Y	Y		Y
NGC 4565	SA(s)b? sp; Sy3, Sy1.9	N		Y				Y
NGC 4594	SA(s)a; LINER,Sy1.9	Y		Y	Y			Y
NGC 4631	SB(s)d; H II	N						N
NGC 4666	SABc:; H II, LINER	Y		Y	Y			Y
NGC 4845	SA(s)ab sp; H II, LINER	Y		Y	Y		Y	Y
NGC 5084	S0; poss. LINER	⋯	Y	Y	Y	Y		Y
NGC 5297	SAB(s)c: sp	⋯		Y		Y?		Y
NGC 5775	Sb(f)	N						N
NGC 5792	SB(rs)b; H II	⋯						N
NGC 5907	SA(s)c: sp; H II	N						N
UGC 10288[j]	Sc	⋯	⋯	⋯	⋯	⋯	⋯	⋯

Notes. Radio data were measured from the rob 0 weighted maps.
[a] Galaxy classification and "activity type" from NED using the classic interface. Some of these entries have been updated since Irwin et al. (2012a).
[b] Galaxies for which *XMM-Newton* spectra suggest an AGN are designated "Y" and shown in Figure 5. Galaxies for which *XMM-Newton* data do not clearly detect an AGN are designated "N," and "⋯" indicates that no data are available. See also Stein et al. (2019a) for details on NGC 4666.
[c] Galaxies that have a flat spectral index near the nucleus (Section 5.1.4 and Table 9).
[d] Galaxies with nuclear point-like cores (Section 5.1.1 and Table 7).
[e] Galaxies that have a nuclear luminosity that exceeds what is normally expected for SNRs (Section 5.1.2 and Tables 7 and 8).
[f] Galaxies showing evidence for radio lobes (Section 5.1.3).
[g] Galaxies showing circular polarization (Irwin et al. 2018).
[h] Final summary of AGN candidates based on radio criteria.
[i] Emission too weak for measurements near the core.
[j] Emission confused with background source (Irwin et al. 2013).

5.2. XMM-Newton *Spectra*

As noted in Section 2.2, we have obtained new *XMM-Newton* data for 19 CHANG-ES galaxies. Of these galaxies, eight show evidence from their X-ray emission of having an AGN (see Figure 5). The 19 galaxies are designated "Y" or "N" in Table 10.

XMM-Newton data may simply not have the capability (sensitivity and resolution) to clearly detect the AGN in some "N" galaxies. A scan through Table 10 illustrates that a number of galaxies that show evidence for a radio AGN do not always show an AGN from the *XMM-Newton* data. For example, the "N" galaxy, NGC 660, clearly harbors an AGN (Argo et al. 2015; Saikia et al. 2018, and CHANG-ES data), as do NGC 3079 and others in this list.

Spectra of two galaxies, NGC 4388 and NGC 4666, as mentioned in Section 2.2, show an iron Fe–Kα line around 6.4 keV, which is a direct argument for the existence of an AGN (e.g., Guainazzi et al. 2005, and references therein).

In two more galaxies, NGC 2683 and NGC 2992, a hint for such a line is visible in their spectra, although no reliable model fit of this line could be performed. Nevertheless, for these two galaxies, as for several other objects, a significant level of hard emission (above 2 keV) can be observed (see Figure 5), suggesting strong nonthermal source(s) of X-ray radiation in

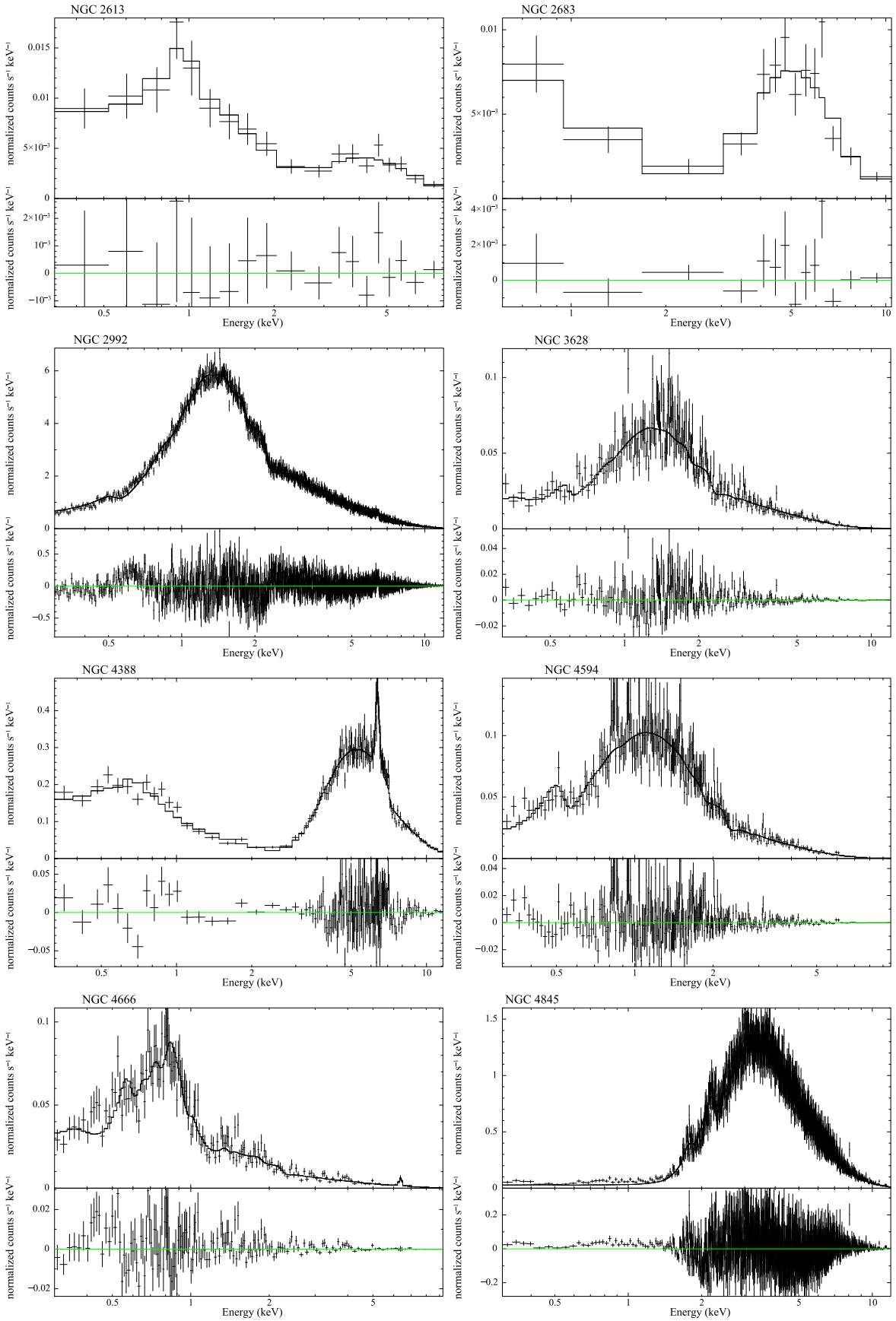

Figure 5. Spectra of the X-ray-selected AGNs. Data are points with error bars, and curves are the best-fit model. Bottom panels show the residuals (data–model).

the galactic core. Although the resolution of the observations does not allow us to clearly determine that this emission comes from a single central source, we can still assume that it contributes significantly to the observed hard X-ray emission. This seems to be justified because typically we expect AGN luminosities of the order of 10^{40} erg s^{-1} or more, while galactic X-ray binaries show only moderate hard emission and have luminosities of 10^{38}–10^{39} erg s^{-1} (see, e.g., Weżgowiec et al. 2016). Therefore, luminosities derived by us and presented in Table 5 are a reliable estimate for each galaxy, most likely agreeing with the real AGN luminosity within the presented uncertainty.

For the galaxies NGC 2613 and NGC 2683, the poor quality of the extracted spectrum, resulting from short observations and lower apparent brightness, caused large uncertainties of the derived luminosity values (Table 5). Nevertheless, the overall spectral distribution of the X-ray emission, with the significant part in the hard range, suggests that these might indeed be luminous AGN-type sources. For a clear confirmation, more sensitive data are certainly needed, especially since in the spectrum of NGC 2683 a hint for an iron Fe–Kα line can be seen, as mentioned above.

We note here that the candidate AGNs presented in Figure 5 have the highest X-ray luminosities (see Table 5) of the studied galaxy sample.

5.3. The Incidence of AGNs in the CHANG-ES Sample

Table 10 summarizes the evidence for AGNs in the CHANG-ES sample. A "Y" in the final column refers to galaxies for which the *radio* criteria point to an AGN.

Galaxies for which only a single radio criterion suggests AGN activity are NGC 3432 and NGC 4565, and therefore these could be considered to be the weaker cases. However, both of these galaxies have been optically identified as either LINERs or Seyferts, strengthening the case for an AGN for these galaxies.

The galaxies that have a single "Y" plus a question mark in the "Lobe(s)" column are NGC 3556 and NGC 5297. For NGC 3556, Satyapal et al. (2008) find no optical evidence for an AGN, but Wang et al. (2003) have identified a possible AGN candidate from X-ray observations. As for NGC 5297, we know of no independent evidence for an AGN, nor is there an NED nuclear classification for this galaxy. These two galaxies are new AGN candidates, i.e., galaxies that have previously been specified as having only an H II-type nuclear spectrum.

The remaining new detection is NGC 2613, which has a point core with a flat spectrum. Even though only a few SNRs could account for the luminosity of the emission (Table 7), the very flat spectrum ($\alpha = -0.1$, Table 9) is unlikely to result from a collection of SNRs. The spectrum is consistent with thermal emission alone, but we would then require a collection of H II regions right at the galaxy's nucleus without SNRs. Finally, the *XMM-Newton* data show a hard spectrum, confirming our conclusion from the radio criteria.

It is interesting that all galaxies for which the X-ray data suggest an AGN (Figure 5) have also been identified as having an AGN via our radio criteria. The converse, however, is not true. This could be because of the resolution of the *XMM-Newton* data, but given the fact that these data are capable of identifying AGNs in many of our other sources, the mismatch could be because of outburst timescales; for example, an X-ray decline could occur in advance of a radio decline.

Several galaxies with known or suspected nuclear activity have been missed using our criteria, namely, NGC 4013, NGC 4192, and NGC 4302. All three galaxies have very strong centrally concentrated radio emission (see Figure 1 and its online figure set, which, nevertheless, is somewhat resolved; see also Stein et al. 2019b, for details of NGC 4013). They also have steep nuclear spectral indices. The same is true for the corresponding CC data at similar resolution. These three galaxies may have been missed because of our strict AGN requirement for an unresolved nuclear radio source. It is likely that a radio AGN is indeed embedded in other emission and the steep spectral indices are the result of masking by the other emission, similar to what was found for NGC 4438 (Section 5.1.3 and Figure 4). Higher-resolution radio observations are recommended for these galaxies.

Our detection rate (excluding the three galaxies noted in the above paragraph) is 18/33, or 55%. We take this as a lower limit to the AGN detection rate in our sample based on radio criteria alone. Note that the selection criteria for CHANG-ES galaxies (Irwin et al. 2012a) did not include any reference to galaxies with AGNs, nor did it favor the inclusion of AGNs. If we include the three galaxies for which independent evidence exists for an AGN, then the detection rate of AGNs among "normal" nearby spiral galaxies is 64%.

Chandra observations by She et al. (2017a) and She et al. (2017b) suggest that the incidence of AGNs in nearby galaxies ranges from 60% in elliptical galaxies to 20% in Sc and later types, and they find 314 AGN candidates that had previously only been designated as H II region-type nuclear spectra. Although we have many fewer galaxies, our detection rate is roughly consistent with She et al. (2017b; see their Table 1), in which they find about 50% in S0 to 39% in Sc and later types for nearby galaxies.

She et al. identify AGN candidates by finding those galaxies that have an X-ray point source at the location of the galaxy center. Their AGN candidates include the CHANG-ES galaxies NGC 891, NGC 3877, NGC 4217, and NGC 5775, for which we find no evidence for a radio AGN. It is possible that their list may have been overestimated (see, e.g., Hodges-Kluck et al. 2018, for NGC 891). However, an intriguing notion is that a radio AGN with sufficiently high luminosity for detection has yet to emerge after an X-ray detection. A detailed investigation of the radio/X-ray connection in AGNs for the CHANG-ES sample is beyond the scope of this paper, but the association between radio and X-ray emission in AGNs (e.g., Panessa et al. 2014), as well as LLAGNs (Su et al. 2017), is well established.

6. High-resolution In-disk Emission in CHANG-ES Galaxies

An abundance of information is available from the high-resolution BL data, and to help in understanding the origin of the discrete radio emission, we provide overlays of radio emission on Hα maps obtained by Vargas et al. (2019; Figure 1, panel (g)). The Hα maps, in standard FITS format, have been presented in Data Release 2. In this section, we examine only two issues of relevance to high-resolution in-disk emission.

6.1. Flat Spectral Indices in the Disks of CHANG-ES Galaxies

In Section 3.4.2, we noted that the thermal component is typically about 8% of the total emission at *L* band. However,

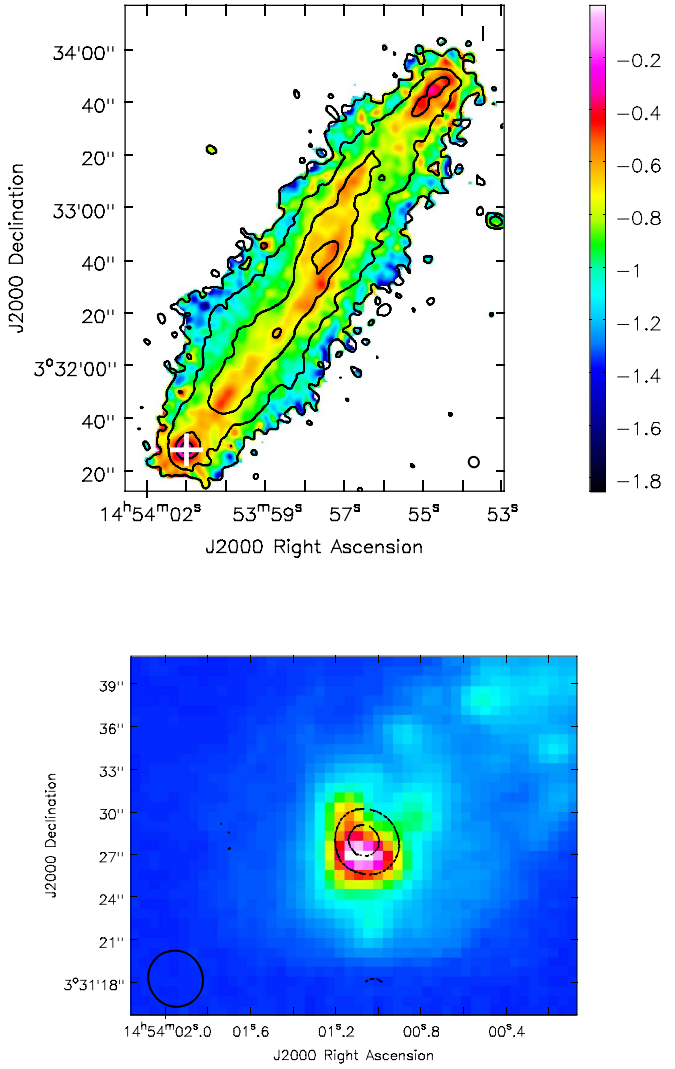

Figure 6. NGC 5775. Top: total intensity BL rob 0 contours over spectral index image with color scale shown at right. The beam of the spectral index image is shown in the lower right corner. Contours are at 42 ($3\sigma_I$), 150, 500, and 1400 μJy beam^{-1}. The H II region complex discussed in Section 6.1 is at the far SE of the disk and denoted with a plus sign. Bottom: blow-up of the SE H II region complex showing two dashed spectral index contours ($\alpha = -0.3$ and -0.25; the latter is smaller) over the Hα image from Collins et al. (2000) in color. The Hα pixel size is $0\farcs68$. The spectral index beam size is shown in the lower left corner.

since the resolution of our BL data is of order a few hundred parsecs (Tables 7 and 8), specific H II regions or H II region complexes in the disk could be resolved as discrete objects. In such regions, nonthermal emission from SNRs can still be important, but the thermal contribution could also be significant. In fact, various CHANG-ES galaxies show many regions of flat spectral index in the disk far from the nucleus. Such regions in the disk obviously cannot be attributed to AGNs.

We consider only one example, the galaxy NGC 5775, and examine a region of relatively flat spectral index far out in its disk, marked with a plus sign in Figure 6 (top: total intensity BL contours over $\alpha_{\rm BL-CC}$ in color). A blow-up of this region is displayed in the same figure (bottom: $\alpha_{\rm BL-CC}$ contours over an Hα image in color). Here the mean spectral index in a region of $\approx$546 pc in diameter (FWHM beam size) is $\alpha_{\rm BL-CC} = -0.26 \pm 0.01$, where the error is also an average over the beam applying the (in this case negligible) corrections of Appendix A. Emission from purely thermal gas should give a flatter spectral index ($I_\nu \propto \nu^{-0.1}$), and emission from purely nonthermal gas (e.g., a collection of SNRs) should give steeper spectral indices, on average ($\alpha \approx -0.7$; see Section 5.1.4 for examples). We consider possible explanations below. In the following, we designate the observed $\alpha_{\rm BL-CC}$ as simply α.

6.1.1. Flattening of the Spectral Index due to Foreground Thermal Absorption

Here we consider nonthermal emission whose spectral index is flattened by thermal absorption from a foreground screen of thermal gas.

Free–free absorption requires an EM of 5×10^7 pc cm^{-6} for a thermal optical depth $\tau_{\nu \rm TH} = 1$ at 3.8 GHz with electron temperature $T_e = 10^4$ K (Equation (7) below). The corresponding electron density would have to be $n_e \approx 300$ cm^{-3} throughout a line of sight equal to the diameter of the region (546 pc). However, we require thermal absorption from a foreground, in which case the line of sight should be reduced and the density correspondingly increased (e.g., a factor of 2 decrease in distance corresponds to a factor of $\sqrt{2}$ increase in density). These are extreme values for the far "edge" of a disk, although other exceptional extragalactic H II regions do exist. For example, 30 Doradus shows a wide range of densities in complex structures (e.g., Scowen et al. 1998; Tsamis & Péquignot 2005), with typical values of $\approx$100 cm^{-3} and much higher densities in smaller filaments (Pellegrini et al. 2010).

A lower but significant optical depth could also flatten the spectral index. For example, for the same parameters but instead using $n_e = 150$ cm^{-3} ($\tau = 0.25$), if the nonthermal spectral index were $\alpha_{\rm NT} = -0.76$, the observed spectral index would be flattened to the observed value of $\alpha = -0.26$ (see Irwin et al. 2015, their Equation (56)).

However, we have stronger constraints available on the spectral index from the observed *in-band* spectral indices at *L* band (over a 512 MHz bandwidth) and at *C* band (2 GHz bandwidth). Although these in-band spectral indices have a lower S/N, they are still sufficiently accurate for comparison (e.g., the BL S/N at this location is >100/1). We find that the observed α at *both* *L* band and *C* band agree with the band-to-band value within errors. That is, the observed spectral index is constant from *L* band through *C* band.

We can now ask what the nonthermal spectral index would be at each frequency if $n_e = 150$ cm^{-3} so that the observed spectral index remains constant at -0.26. We find that we require $\alpha_{\rm NT} = -3.4$ within *L* band, $\alpha_{\rm NT} = -0.75$ band to band (as calculated above), and $\alpha_{\rm NT} = -0.45$ within *C* band. In other words, $\alpha_{\rm NT}$ would have to be strongly varying with frequency in order for the observed value to remain constant. This scenario seems highly unlikely, and we therefore rule out thermal absorption as the cause of a relatively flat spectral index at the location of the SE H II region in NGC 5775.

6.1.2. Flattening of the Spectral Index due to a Thermal Contribution

Here we consider that α has been flattened because of an optically thin thermal emission fraction that is higher than the estimated global values of 8% at *L* band and 20% at *C* band (Section 3.4.2).

Then, with NT and TH referring to nonthermal and thermal quantities, respectively, and *I* being the specific intensity, the

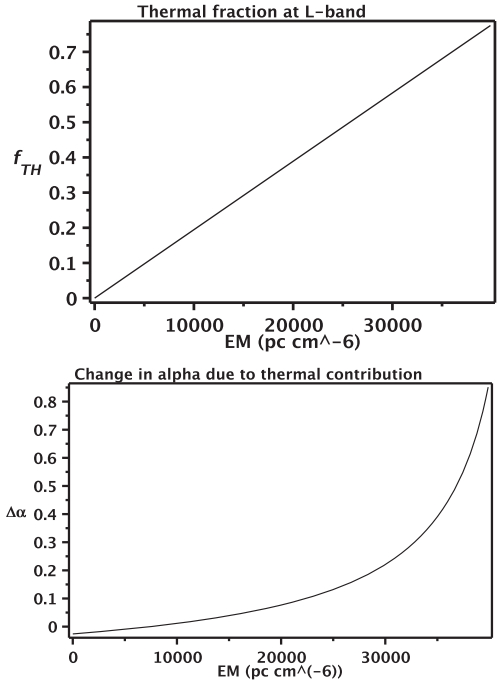

Figure 7. Thermal fraction $f_{\nu_{\rm TH}}$ at L band (top) and change in spectral index $\Delta\alpha = \alpha - \alpha_{\rm NT}$ (bottom) at 3.8 GHz that results from a range of emission measures EM (see Section 6.1).

standard equations are

$$I_{\nu_{\rm obs}} = K\nu^{\alpha} = I_{\nu_{\rm NT}} + I_{\nu_{\rm TH}} \quad (5)$$

$$= C\nu^{\alpha_{\rm NT}} + \left(\frac{2\nu^2 k}{c^2}\right) T_e \tau_{\nu_{\rm TH}}, \quad (6)$$

where K and C are constants, k and c are Boltzmann's constant and the speed of light, respectively, and we have employed the Rayleigh–Jeans relation in Equation (6). We have two sets of equations, one for each of BL and CC data at matching resolutions. The thermal optical depth is well known, i.e.,

$$\tau_{\nu_{\rm TH}} = 8.24 \times 10^{-2}\left[\frac{T_e}{\rm K}\right]^{-1.35}\left[\frac{\nu}{\rm GHz}\right]^{-2.1}\left[\frac{\rm EM}{\rm pc\ cm^{-6}}\right]. \quad (7)$$

For an adopted value of EM (assuming $T_e = 10^4$ K), $I_{\nu_{\rm TH}}$ is easily calculated, and $I_{\nu_{\rm NT}}$ is obtained from Equation (5), from which the thermal fraction $f_{\nu_{\rm TH}} = I_{\nu_{\rm TH}}/I_{\nu_{\rm obs}}$ follows for each band. With $I_{\nu_{\rm NT}}$ at both bands, the nonthermal spectral index $\alpha_{\rm NT}$ is found along with the difference $\Delta\alpha = \alpha - \alpha_{\rm NT}$. The latter quantity indicates how much the spectrum has been flattened by the addition of thermal emission.

Figure 7 shows the thermal fraction at L band and $\Delta\alpha$ at 3.8 GHz (corresponding to the midpoint between the L-band and C-band observations) for a variety of values of EM. As the contribution of thermal gas increases, so does $\Delta\alpha$. For example, if $\alpha_{\rm NT} = -0.72$ at 3.8 GHz, then $\Delta\alpha = 0.46$, EM $= 3.62 \times 10^4$ pc cm^{-6}, and $f_{\rm th} = 0.7$ at L band and $f_{\rm th} = 0.8$ at C band. The thermal gas is highly optically thin at both frequencies. The average electron density over the line of sight would be $n_e = 8$ cm^{-3}. Unlike the case for thermal absorption (Section 6.1.1), the nonthermal spectral index does not vary with frequency, and we can clearly see that the required electron density is a more moderate value.

We finally can compare the emission measure with the observed value of 2958 cm^{-6} pc obtained from the Hα image (Collins et al. 2000). Figure 7 shows that such a low value of EM would produce only a negligible amount of spectral flattening. Thus, either $\alpha_{\rm NT}$ is quite flat to begin with, or the optically measured EM is heavily extincted by dust. We suspect the latter and suggest that further analysis of this region to determine the dust contribution would provide such verification.

In summary, flat spectral indices in discrete regions in the disks of the CHANG-ES galaxies are most likely due to a higher-than-average contribution from thermal emission.

6.2. Background Sources

At L band, there are many background sources in the various fields. We note that since 35 fields at each of two different *uv* weightings are available, the BL images can provide an independent measurement set for source count studies. With rms values typically of order 20 μJy beam^{-1} (Table 2), the CHANG-ES data can provide source count estimates to very low levels (though subject to PB weighting). In addition, our matching resolution CC data set (R. Walterbos et al. 2019, in preparation) has rms values that are typically much less than 10 μJy beam^{-1}. In this section we consider only the possibility that background sources may be seen through the disks of our galaxies.

Numerous studies have examined radio source counts historically, and more recently to increasingly lower flux levels, especially in anticipation of the full power of the SKA.[19] Unfortunately, considerable scatter is seen in the differential source counts at the lowest flux levels. For example, the 1.4 GHz normalized differential source counts vary by a factor of ≈6 at a level of 100 μJy (De Zotti et al. 2009; Prandoni et al. 2018), underscoring the need for good deep surveys.

More relevant to an analysis of the edge-on galaxies is how many background sources might be shining through the galaxy disks. Such sources may need to be removed before detailed analysis of the galaxies can be carried out.

We have several clear examples of known background sources seen through the disk. An example is NGC 5907, which has a very strong double-lobed radio source behind the far SE tip of the major axis (Dumke et al. 2000) as can clearly be seen in Figure 1 and its online figure set. In this case, the extragalactic nature of the source is obvious, and its spectral index is also discordant compared to the galaxy's disk. Another example is UGC 10288 (Figure 1 and its online figure set), whose radio emission is actually dominated by the background double-lobed radio source as described in detail in Irwin et al. (2013).

However, sources such as the point source at R.A. = $12^{\rm h}13^{\rm m}47\overset{\rm s}{.}1$, decl. = $14^{\rm h}54^{\rm m}49\overset{\rm s}{.}2$, apparently in the disk of NGC 4192 (Figure 1 and its online figure set) with a peak specific intensity of 0.60 mJy beam^{-1}, may or may not be a background source.

Bearing in mind the uncertainties noted above, one can make a rough estimate of the number of sources that might be seen through the disk of such a galaxy. Following Rahman (2016), who employed the simulations of Wilman et al. (2008), we would expect ≈108 background sources to be present in any $1000'' \times 1000''$ field above a typical 3σ threshold of 60 μJy

[19] Square Kilometre Array.

beam^{-1}. For the specific NGC 4192 field (rob 0), taking an ellipse for the galaxy area of major-axis × minor-axis size, 250″ × 45″, and adopting a more stringent 5σ limit of 87 μJy beam^{-1} for that field, we then expect 0.6 background sources to be shining through the disk. For NGC 4192, then, the point source noted above could indeed be a background source. Higher-resolution observations are really required to confirm this.

7. Summary and Conclusions

We have now presented the third data release of the CHANG-ES galaxy sample of 35 edge-on nearby galaxies. This data release consists of FITS images at 1.58 GHz taken in the B configuration (BL data) of the VLA with a spatial resolution of ≈3″. For most galaxies, *uv*-tapered images with a resolution of ≈6″ were also made and are in the data release. In addition to these images, we include band-to-band spectral index maps made from BL and C configuration 6.00 GHz data (CC data) at matching spatial resolutions.

In-band spectral indices (over 512 MHz *L*-band bandwidth and 2 GHz bandwidth at *C* band) have been made but are not released, given the relatively low S/N for many galaxies. Polarization at *L* band is not detected except for two galaxies, NGC 3079 and NGC 4388 (Figure 2), because of Faraday depolarization at *L* band; consequently, polarization images are also not included in the data release. Nonrelease images for this configuration can be requested from the first author, if required. Otherwise, release data can be downloaded from https://www.queensu.ca/changes.

Panels displaying the data products are provided in Figure 1 and its online figure set for all galaxies. The C configuration data from which the spectral index maps were made will be released separately (R. Walterbos et al. 2019, in preparation), and the Hα images that are displayed in the panels can already been downloaded from our data release website (see Vargas et al. 2019).

Several new and unique results have been identified. We see structures in the spectral index maps that are not observed in total intensity, presumably because the structure is swamped by other emission in total intensity. An example is apparent spiral arms in NGC 3448 and two radio lobes on either side of the nucleus in NGC 3628. Thus, high-resolution spectral index maps are essential for revealing otherwise hidden features and show us how the energy spectral index of cosmic-ray electrons varies with position.

We have looked for radio-only criteria for identifying AGNs in these galaxies, including unresolved point-like cores, high radio luminosities, radio lobes, and relatively flat spectra in the cores. Other criteria, such as time variability, circular polarization, and high brightness temperatures, have been examined elsewhere or are not applicable to this data set (Section 5.1). We find a lower limit to the incidence of radio AGNs of 55% in nearby spiral galaxies. This incidence increases to 64% if we include galaxies that have strongly peaked emission in the core but for which emission is still slightly resolved.

All galaxies for which available X-ray data suggest the presence of an AGN are also radio AGNs. However, some other galaxies (e.g., NGC 660 and NGC 3079) clearly have radio AGNs but show only little evidence for an X-ray AGN. This could be because of timescales, with the X-ray emission fading before the radio, or could be related to the resolution and sensitivity of the *XMM-Newton* data.

An examination of discrete emission in galaxy disks reveals some regions of quite flat spectral index, which can reasonably be explained by a contribution from free–free thermal emission that is higher than the global average. We suggest that one such H II region in the outer disk of NGC 5775 could have a thermal fraction of as much as 70% at *L* band. A careful comparison between the Hα images and the radio continuum will likely prove to be of importance for other discrete regions, provided that dust obscuration is also considered carefully.

The *L*-band fields contain many background sources, some of which may be shining through the disks of the nearby galaxies.

The first author would like to thank the Natural Sciences and Engineering Research Council of Canada for a Discovery Grant. The National Radio Astronomy Observatory is a facility of the National Science Foundation operated under cooperative agreement by Associated Universities, Inc. This research has made use of the NASA/IPAC Extragalactic Database (NED), which is operated by the Jet Propulsion Laboratory, California Institute of Technology, under contract with the National Aeronautics and Space Administration.

Facility: VLA.

Appendix A
Corrections to the Spectral Index Error Maps

For highest accuracy, the spectral index error maps should take into account the fact that the rms noise increases with distance from the field (pointing) center. The corrected uncertainty is

$$\sigma_{\alpha\mathrm{corr}} = \frac{1}{\ln\left(\frac{\nu_L}{\nu_C}\right)}\sqrt{\left(\frac{\sigma_L}{\mathrm{PB}_L(r)I_L}\right)^2 + \left(\frac{\sigma_C}{\mathrm{PB}_C(r)I_C}\right)^2}, \quad (8)$$

where $\mathrm{PB}_L(r)$ and $\mathrm{PB}_C(r)$ are the primary beam responses at *L* band and *C* band, respectively, and *r* is the distance from the field center. Rearranging this equation and using Equation (3) to eliminate I_L and I_C, we find

$$\sigma_{\alpha\mathrm{corr}} = \frac{\sigma_L}{I_L \ln\left(\frac{\nu_L}{\nu_C}\right)}\sqrt{\frac{1}{(\mathrm{PB}_L(r))^2} + \frac{1}{(\mathrm{PB}_C(r))^2}\left(\frac{\sigma_C}{\sigma_L}\right)^2\left(\frac{\nu_L}{\nu_C}\right)^{2\alpha}}. \quad (9)$$

The primary beam shape, PB(*r*), is given in Perley (2016) as a sixth-order polynomial. However, for the regions shown in our spectral index maps, the polynomial is well fitted by a normalized Gaussian, where the half-width at half-maximum (HWHM) is 12.′76 at 1.57 GHz and 3.′51 at 6.00 GHz, i.e.,

$$\mathrm{PB}_L(r) = e^{\left(-\frac{1}{2}\left(\frac{r}{10.8}\right)^2\right)} \quad \mathrm{PB}_C(r) = e^{\left(-\frac{1}{2}\left(\frac{r}{2.98}\right)^2\right)}, \quad (10)$$

where *r* is in units of arcmin and the standard deviation $\sigma = 10.8$ for an HWHM of 12.76 and $\sigma = 2.98$ for an HWHM of 3.51 in the same units.

Thus, given an input spectral index map, α, Equation (9) together with Equation (10) can be used to determine a corrected value of the error in the spectral index. The quantities σ_L and σ_C are taken as constant for a given map and are read

from Table 6, whereas α varies with position and the PBs are functions of r.

Alternatively, the given error maps can be corrected by multiplying by a factor

$$f(r) = \frac{\sigma_{\alpha\mathrm{corr}}}{\sigma_\alpha} = \sqrt{\frac{\frac{1}{(\mathrm{PB}_L(r))^2} + \frac{1}{(\mathrm{PB}_C(r))^2}\left(\frac{\sigma_C}{\sigma_L}\right)^2 (0.26)^{2\alpha}}{1 + \left(\frac{\sigma_C}{\sigma_L}\right)^2 (0.26)^{2\alpha}}}, \quad (11)$$

where σ_α is given by Equation (4) and we have explicitly evaluated the frequency ratio for CHANG-ES.

For example, let $r = 3'$, $\alpha = -0.8$, $\sigma_L = 16\ \mu$Jy beam^{-1}, and $\sigma_C = 3\ \mu$Jy beam^{-1}. Then $\mathrm{PB}_L(r) = 0.96$, $\mathrm{PB}_C(r) = 0.60$, and $f(r) = 1.2$. At the adopted position, the error map value would be increased by this factor.

Appendix B
Galaxy Panels

Figure 1 and its online figure set display images of the data products in Data Release 3 of the CHANG-ES project, described below. Each field of view is the same for any given galaxy. Missing panels may occur if images were not satisfactorily made (e.g., *uv*-tapered).

For the large galaxies, NGC 891, NGC 4565, and NGC 5907, in addition to the complete panels, we include blow-ups of panels (a), (b), (g), and (h) as described below.

First row:

(a) Contours and a color scale (logarithmically stretched from background (2σ) to peak emission) for total intensity images with a Briggs robust = 0 (rob 0) *uv* weighting. The I contours are at 3, 6, 12, 24, 48, 96, and 192 times the rms value. The rms values are taken from Table 2, where the higher value near the galaxy has been used in cases where there is strong variation.

(b) Same as (a), except that these maps are total intensity images with a *uv* taper applied onto the rob 0 weighting (Section 2.1 and Table 2).

Second row:

(c) Band-to-band (BL to CC) spectral index maps for rob 0 weighting. A cutoff of 3 times the rms value has been applied to each map (both BL and CC) as described in Section 3.4. In this case, the rms values for each band are listed in Table 6. The color scheme is displayed to the right of panel (d). These maps tend to look noisier than the others because the PB correction for each band results in an increasing rms with distance from the map center (Section 3.4). Note that no correction for thermal emission has been made (Section 3.4.2).

Note that care has been taken for the color scheme. We show flatter spectral indices as dark blue-purple, and steeper spectral indices appear orange-yellow. Thus, flatter regions, such as those containing AGNs (synchrotron dominated) or discrete H II regions (thermal dominated), may be identified by their blue-purple color. Regions in which diffuse synchrotron emission dominates will appear orange or even yellow if the spectral index is very steep.

(d) Same as panel (c), but for the rob 0 maps with a *uv* taper.

Third row:

(e) Spectral index uncertainty map corresponding to panel (c). The color scheme is displayed to the right of panel (f). See Section 3.4.1 for a discussion of the uncertainties and Appendix A for corrections with distance from the center.

(f) Same as panel (e), but for the rob 0 maps with a *uv* taper.

Fourth row:

(g) Same contours as in (a) over a color Hα image from Vargas et al. (2019); log stretch from background to peak emission). Hα FITS images are available on our data release website (see Section 6).

(h) The 3σ contour from (b) over an optical image of the galaxy. When panel (b) is unavailable, we use the 3σ contour from panel (a) instead. The optical images were created using a combination of Sloan Digital Sky Survey (SDSS) *g*, *r*, and *i* bands *or* Digitized Sky Survey 2 (DSS2) blue, red, and infrared bands, for the galaxies not available in SDSS.

ORCID iDs

Judith Irwin https://orcid.org/0000-0002-2046-6727
Theresa Wiegert https://orcid.org/0000-0002-3502-4833
Ancor Damas-Segovia https://orcid.org/0000-0002-5747-8510
Q. Daniel Wang https://orcid.org/0000-0002-9279-4041

References

Adebahr, B., Krause, M., Klein, U., et al. 2013, A&A, 555, A23
Allen, M. L., & Kronberg, P. 1999, ApJ, 502, 218
Argo, M. K., van Bemmel, I. M., Connoll, S. D., & Beswick, R. J. 2015, MNRAS, 452, 1081
Arnaud, K. A. 1996, in ASP Conf. Ser. 101, Astronomical Data Analysis Software and Systems V, ed. G. Jacoby & J. Barnes (San Francisco, CA: ASP), 17
Bell, A. R., Schure, K. M., & Reville, B. 2011, MNRAS, 418, 1208
Briggs, D. 1995, PhD thesis, New Mexico Institute of Mining and Technology
Carlstrom, J. E., & Kronberg, P. P. 1991, ApJ, 366, 422
Carter, J. A., & Read, A. M. 2007, A&A, 464, 1155
Collins, J. A., Rand, R. J., Duric, N., & Walterbos, R. A. M. 2000, ApJ, 536, 645
Contini, M. 2011, MNRAS, 418, 1935
Cornwell, T. J., Golap, K., & Bhatnagar, S. 2008, ISTSP, 2, 647
Damas-Segovia, A., Beck, R., Vollmer, B., et al. 2016, ApJ, 824, 30
De Zotti, G., Massardi, M., Negrello, M., & Wall, J. 2009, A&ARv, 18, 1
Desouza, A. MSc thesis, Queen's Univ., https://qspace.library.queensu.ca/handle/1974/22823
Dumke, M., Krause, M., & Wielebinski, R. 2000, A&A, 355, 512
Evans, I. N., Primini, F. A., Glotfelty, K. J., et al. 2010, ApJS, 189, 37
Everett, J. E., & Weisberg, J. M. 2001, ApJ, 553, 341
Gabriel, C., Denby, M., Fyfe, D. J., et al. 2004, in ASP Conf. Ser. 314, Astronomical Data Analysis Software and Systems (ADASS) XIII, ed. F. Ochsenbein, M. G. Allen, & D. Egret (San Fransisco, CA: ASP), 759
Grimm, H.-J., Gilfanov, M., & Sunyaev, R. 2003, MNRAS, 339, 793
Guainazzi, M., Matt, G., & Perola, G.-C. 2005, A&A, 444, 119
Gültekin, K., Cackett, E. M., King, A. L., Miller, J. M., & Pinkney, J. 2014, ApJ, 788L, 22
Ho, L. C. 2009, ApJ, 699, 626
Ho, L. C., Filippenko, A. V., & Sargent, W. L. W. 1997, ApJS, 112, 315
Hodges-Kluck, E. J., Bregman, J. N., & Li, J. 2018, ApJ, 866, 126
Hota, A., Saikia, D. J., & Irwin, J. 2007, MNRAS, 380, 1009
Hummel, E., van Gorkom, J. H., & Kotznyi, C. G. 1984, ApJL, 267, L5
Hummerl, E., & Saikia, D. J. 1991, A&A, 249, 43
Irwin, J., Beck, R., Benjamin, R. A., et al. 2012a, AJ, 144, 43
Irwin, J., Beck, R., Benjamin, R. A., et al. 2012b, AJ, 144, 44
Irwin, J., Henriksen, R., Krause, M., et al. 2015, ApJ, 809, 172
Irwin, J., Henriksen, R., Weżgowiec, M., et al. 2018, MNRAS, 476, 5057
Irwin, J., Krause, M., English, J., et al. 2013, AJ, 146, 164
Irwin, J., Schmidt, P., Damas-Segovia, A., et al. 2017, MNRAS, 464, 1333
Kaastra, J. S. 1992, Internal SRON-Leiden Report, updated version 2.0
Kalberla, P. M. W., Burton, W. B., Hartmann, D., et al. 2005, A&A, 440, 775
Kronberg, P. P., & Sramek, R. A. 1992, in MPE Conf. 235, X-Ray Emission from Active Galactic Nuclei and the Cosmix X-ray Background, ed. W. Brinkman & J. Trumper (Garching: MPI), 247
Kronberg, P. P., & Wilkinson, P. N. 1975, ApJ, 200, 430
Lee, S.-W., Irwin, J. A., Dettmar, R.-J., et al. 2001, A&A, 377, 759
Longair, M. S. 1994, High Energy Astrophysics, Vol. 2 (2nd ed.; Cambridge: Cambridge Univ. Press)

Maoz, D. 2008, JPhCS, 131, 012036
McDonald, A. R., Muxlow, T. W. B., Wills, K. A., et al. 2002, MNRAS, 334, 21
Mewe, R., Bronenschild, E. H. B. M., & van den Oord, G. H. J. 1985, A&AS, 62, 197
Morrison, R., & McCammon, D. 1983, ApJ, 270, 119
Muxlow, T. W., Pedlar, A., Wilkinson, P. N., et al. 1994, MNRAS, 266, 455
Nagar, N. M., Falcke, H., & Wilson, A. S. 2005, A&A, 435, 521
Onić, D., Urošević, D., Arbutina, B., & Leehy, D. 2012, ApJ, 756, 61
Panessa, F., Tarchi, A., Castangia, P., et al. 2014, MNRAS, 447, 1289
Pellegrini, E. W., Baldwin, J. A., & Ferland, G. E. 2010, ApJS, 191, 160
Perley, R. 2016, EVLA Memo 195, Jansky Very Large Array Primary Beam Characteristics, https://library.nrao.edu/public/memos/evla/EVLAM_195.pdf
Perley, R. A., & Butler, B. J. 2013, ApJS, 204, 19
Prandoni, I., Guglielmino, G., Morganti, R., et al. 2018, MNRAS, 481, 4548
Rahman, S. F. 2016, arXiv:1612.08226v8
Rau, U., & Cornwell, T. J. 2011, A&A, 532, A71
Reynolds, S. P., Borkowski, K. J., Green, D. A., et al. 2008, ApJ, 680, L41
Saikia, P., Körding, E., Coppejans, D. L., et al. 2018, A&A, 616, A152
Satyapal, S., Vega, D., Dudik, R. P., Abel, N. P., & Heckman, T. 2008, ApJ, 677, 926
Sault, R. J., & Conway, J. E. 1999, in ASP Conf Ser. 180, Synthesis Imaging in Radio Astronomy II, ed. G. B. Taylor, C. L. Carilli, & R. A. Perley (San Francisco, CA: ASP), 419
Schwab, F. R. 1984, AJ, 89, 1076
Scowen, P. A., Hester, J. J., Sankrit, R., et al. 1998, AJ, 116, 163
Seaquist, E. R., Bell, M. B., & bignell, R. C. 1985, ApJ, 294, 546
She, R., Ho, L. C., & Feng, H. 2017a, ApJ, 835, 223
She, R., Ho, L. C., & Feng, H. 2017b, ApJ, 842, 131
Simmons, J. F. L., & Stewart, B. G. 1985, A&A, 142, 100
Stein, Y., Dettmar, R.-J., Irwin, J., et al. 2019a, A&A, 623, A33
Stein, Y., Dettmar, R.-J., Weżgowiec, M., et al. 2019b, A&A, submitted
Strüder, L., Briel, U., Dennerl, K., et al. 2001, A&A, 365, 18
Su, R., Liu, X., & Zhang, Z. 2017, Ap&SS, 362, 3
Tsamis, Y. G., & Péquignot, D. 2005, MNRAS, 364, 687
Turner, M. J. L., Abbey, A., Arnaud, M., et al. 2001, A&A, 365, 27
Urošević, D. 2014, Ap&SS, 354, 541
Vaillancourt, J. E. 2006, PASP, 118, 1340
Varenius, E., Conway, J. E., Martí-Vidal, I., et al. 2015, A&A, 574, A114
Vargas, C. J., Mora-Partiarroyo, S. C., Schmidt, P., et al. 2018, ApJ, 853, 128
Vargas, C. J., Walterbos, R. A. M., Rand, R. J., et al. 2019, ApJS, in press
Wang, Q. D., Chaves, T., & Irwin, J. A. 2003, ApJ, 598, 969
Weżgowiec, M., Ehle, M., & Beck, R. 2016, A&A, 585, A3
Wiegert, T., Irwin, J., Miskolczi, A., et al. 2015, AJ, 150, 81
Wills, K. A., Pedlar, A., Muxlow, T. W. B., & Wilkinson, P. N. 1997, MNRAS, 291, 517
Wilman, R. J., Miller, L., Jarvis, M. J., et al. 2008, MNRAS, 388, 1335